

1                    **Subsurface oceanic structure associated with**  
2                    **atmospheric convectively coupled equatorial Kelvin**  
3                    **waves in the eastern Indian Ocean**

4                    **Marina do V. C. Azaneu<sup>1</sup>, Adrian J. Matthews<sup>2</sup>, Dariusz B. Baranowski<sup>3</sup>**

5                    <sup>1</sup>Centre for Ocean and Atmospheric Sciences, School of Environmental Sciences, University of East  
6                    Anglia, Norwich, UK

7                    <sup>2</sup>Centre for Ocean and Atmospheric Sciences, School of Environmental Sciences and School of  
8                    Mathematics, University of East Anglia, Norwich, UK

9                    <sup>3</sup>Institute of Geophysics, Polish Academy of Sciences, Warsaw, Poland

10                    **Key Points:**

- 11                    • Atmospheric CCKWs in the eastern Indian Ocean produce a coherent surface and  
12                    subsurface thermodynamic and dynamical ocean response
- 13                    • As a dynamical response to CCKWs, an ocean Kelvin wave propagates along the  
14                    coasts of Sumatra and Java and lasts up to 11 days beyond the forcing
- 15                    • CCKWs lead to a long lived ocean heat content increase through deepening of mixed  
16                    layer and forcing of downwelling oceanic Kelvin wave

---

Corresponding author: Marina do V. C. Azaneu, [m.azaneu@uea.ac.uk](mailto:m.azaneu@uea.ac.uk)

**Abstract**

17 Atmospheric convectively coupled equatorial Kelvin waves (CCKWs) are a major trop-  
18 ical weather feature strongly influenced by ocean–atmosphere interactions. However, pre-  
19 iction of the development and propagation of CCKWs remains a challenge for models.  
20 The physical processes involved in these interactions are assessed by investigating the  
21 oceanic response to the passage of CCKWs across the eastern Indian Ocean and Mar-  
22 itime Continent using the NEMO ocean model analysis with data assimilation. Three-  
23 dimensional life cycles are constructed for “solitary” CCKW events. As a CCKW prop-  
24 agates over the eastern Indian Ocean, the immediate thermodynamic ocean response in-  
25 cludes cooling of the ocean surface and subsurface, deepening of the mixed layer depth,  
26 and an increase in the mixed layer heat content. Additionally, a dynamical downwelling  
27 signal is observed two days after the peak in the CCKW westerly wind burst, which prop-  
28 agates eastward along the Equator and then follows the Sumatra and Java coasts, con-  
29 sistent with a downwelling oceanic Kelvin wave with an average phase speed of  $2.3 \text{ m s}^{-1}$ .  
30 Meridional and vertical structures of zonal velocity anomalies are consistent with this  
31 framework. This dynamical feature is consistent across distinct CCKW populations, in-  
32 dicating the importance of CCKWs as a source of oceanic Kelvin waves in the eastern  
33 Indian Ocean. The subsurface dynamical response to the CCKWs is identifiable up to  
34 11 days after the forcing. These ocean feedbacks on time scales longer than the CCKW  
35 life cycle help elucidate how locally driven processes can rectify onto longer time-scale  
36 processes in the coupled ocean–atmosphere system.  
37

**Plain Language Summary**

38 We investigate the effects that the passage of a weather system (an atmospheric  
39 convectively coupled equatorial Kelvin wave, CCKW) along the Equator has in the east-  
40 ern Indian Ocean. CCKWs can intensify precipitation and cause extreme weather, such  
41 as flooding, over the islands of the Maritime Continent, which include Indonesia and Malaysia.  
42 CCKWs affect the ocean and which can then feedback onto the CCKWs. A better un-  
43 derstanding of the physical processes connecting the atmosphere and ocean during a CCKW  
44 passage is still needed to improve its prediction by models. More accurate CCKW pre-  
45 diction will then help to mitigate some of the consequences of the weather-related nat-  
46 ural disasters in the region. We show that the effects of the passage of the CCKW on  
47 the ocean are relatively long-lived. For example, the increase in the amount of heat avail-  
48

49 able at the ocean surface is maintained for several days after the CCKW has passed. We  
50 also show that CCKWs are also capable of triggering dynamic processes in the ocean that  
51 can influence precipitation over the islands at a later time. These results show that CCKWs  
52 can influence oceanic and weather conditions after their passage and in remote areas, such  
53 as coastal regions.

## 54 **1 Introduction**

55 The equatorial Indian Ocean and its interaction with the atmosphere has an im-  
56 portant role in influencing climate both locally and remotely (Schott et al., 2009). The  
57 region is under the influence of a wide range of modes of variability, with strong multi-  
58 scale interaction between them. In particular, intraseasonal variability is strong in the  
59 equatorial Indian Ocean, which has been linked to atmospheric forcing in its central and  
60 eastern portion (e.g., Han et al., 2001; Han, 2005; Iskandar & McPhaden, 2011). This  
61 intraseasonal oceanic variability, which tends to undergo a shift towards lower frequen-  
62 cies when compared to its atmospheric forcing, can then feed back onto atmospheric dy-  
63 namics through ocean–atmosphere interaction, potentially influencing the evolution of  
64 longer time-scale systems, for example the Indian Ocean Dipole (Rao & Yamagata, 2004).

65 On time scales of a few days, atmospheric convectively coupled Kelvin waves (CCKWs)  
66 are the primary mode of variability of eastward moving convection near the Equator (Wheeler  
67 & Kiladis, 1999; Roundy, 2008; Kiladis et al., 2009) with phase speeds between 11 and  
68  $14 \text{ m s}^{-1}$ . They are accompanied by coherent dynamical atmospheric signals in wind, tem-  
69 perature and humidity (Wheeler et al., 2000) and are theoretically considered as equa-  
70 torial Kelvin waves (Gill, 1980), modified by moist atmospheric convection.

71 CCKWs have a strong interaction with the underlying ocean. Enhanced surface  
72 wind speed and air-sea heat flux, besides anomalous precipitation, characterize the pas-  
73 sage of a CCKW event, which lasts approximately 4 days at a given longitude (Baranowski  
74 et al., 2016a). The localized upper ocean response includes the temporary suppression  
75 of the diurnal cycle of SST and decrease of mean SST by  $0.1\text{--}0.3^\circ\text{C}$  as a result of air-  
76 sea heat loss at the surface and subsurface turbulent mixing (Baranowski et al., 2016a;  
77 Pujiana & McPhaden, 2018). Stratification and mixing are also modulated by surface  
78 fluxes and eastward acceleration of surface layer under intensified winds. Changes in the

79 barrier layer thickness have also been reported, which may potentially limit heat trans-  
80 fer to subsurface layers (Pujiana & McPhaden, 2018).

81 CCKWs increase precipitation along their track and locally, over the islands of the  
82 Maritime Continent, are often phase-locked with the local diurnal cycle of precipitation  
83 with a potential to amplify it (Baranowski et al., 2016b). Therefore, they contribute to  
84 extreme precipitation in the already extremely wet environment of the eastern Indian  
85 Ocean and Maritime Continent, enhancing the likelihood of flooding in islands such as  
86 Sumatra, which is home to over 50 million people (Baranowski et al., 2020). Thus, in  
87 order to help mitigate some of the consequences of weather-related natural disasters and  
88 contribute to the understanding of global climate teleconnections, a deeper understand-  
89 ing of the physical processes involved in the ocean-atmospheric interactions associated  
90 with CCKWs is needed.

91 On larger scales, the dominant mode of intraseasonal variability in the tropical In-  
92 dian Ocean is the Madden–Julian Oscillation (MJO) (Zhang, 2005), which has a broad-  
93 band spectral signal with an energy peak in the 40–60 day range (Madden & Julian, 1971).  
94 The MJO also has a strong coupling with the ocean, both thermodynamically through  
95 surface fluxes (e.g. M. Flatau et al., 1997; M. K. Flatau et al., 2003; Shinoda et al., 1998;  
96 Moum et al., 2016; DeMott et al., 2015), and dynamically. For example, a “primary” Madden–  
97 Julian event can be triggered by the westward propagation of a downwelling Rossby wave  
98 from the eastern Indian Ocean (Webber et al., 2012; Rydbeck & Jensen, 2017).

99 The MJO has an intrinsic multiscale structure (Birch et al., 2016; Hagos et al., 2020).  
100 CCKWs are among the several “building blocks” of the MJO multiscale structure, be-  
101 ing embedded in its large scale convective envelope (Majda et al., 2004; Mapes et al., 2006).  
102 It is hypothesized that the propagation of the MJO envelope over the Maritime Conti-  
103 nent is dependent on the ability of CCKWs to cross this barrier (Inness & Slingo, 2006),  
104 An additional factor that impacts on the MJO being able to cross the Maritime Con-  
105 tinent is its interaction with the diurnal cycle (Ling et al., 2019), which again leaves a  
106 role for CCKWs (Baranowski et al., 2016b).

107 Scale interactions between the MJO and CCKWs can be analysed using the frame-  
108 work of Meehl et al. (2001). The larger scale MJO sets the environment within which  
109 the smaller scale CCKWs develop. The CCKWs then feedback upscale to the MJO through  
110 long-lasting changes to the ocean, and atmospheric humidity. Such a rectification by CCKWs

111 has already been observed through their thermodynamical impact on the ocean, with  
112 sea surface temperature (SST) changes, induced by enhanced latent heat flux from west-  
113 erly wind anomalies associated with CCKWs, persisting well beyond the passage of the  
114 CCKW (Baranowski et al., 2016a).

115 Even though the localized effect of an atmospheric CCKW passage on the surface  
116 and subsurface ocean has been assessed, there is still uncertainty regarding the longer  
117 term effects of this atmospheric forcing in the ocean and their interaction with other modes  
118 of variability. Evaluating the upper ocean variability within the CCKW life span, Baranowski  
119 et al. (2016a) observed residual changes in some properties, suggesting that air-sea flux  
120 variability associated with the passage of a CCKW event may feedback onto longer time  
121 scale weather systems like the MJO, and thus play a key role in the tropical ocean-atmospheric  
122 system. Moreover, feedbacks between precipitation, salt-stratified oceanic barrier lay-  
123 ers and the upper ocean diurnal cycle are likely to play important roles in the multi-scale  
124 interactions between modes of atmospheric convection.

125 This study aims to build on previous work by examining the three-dimensional ocean  
126 response to the passage of CCKWs on different time scales, across the eastern Indian Ocean  
127 basin and the Maritime Continent, using 10 years of an ocean analysis dataset. Section 2  
128 describes the data and methodology used. The composite atmospheric structure of CCKWs  
129 is constructed in Section 4, to inform the thermodynamic and dynamic ocean structures  
130 associated with CCKWs in Section 5. Ocean feedbacks of CCKWs onto the atmosphere  
131 are presented in Section 6, and conclusions in Section 7.

## 132 **2 Data and methodology**

### 133 **2.1 Meteorological datasets**

134 Precipitation was analysed using the Tropical Rainfall Measuring Mission (TRMM)  
135 3B42v7 precipitation product (Huffman et al., 2007), which provides 3-hourly estimates  
136 of precipitation rate on a  $0.25^\circ \times 0.25^\circ$  resolution grid (approximately 28 km in the trop-  
137 ics). The analysis period for TRMM and all other variables was the 11 years from 1 Jan-  
138 uary 2007 to 31 January 2017.

139 The TropFlux product (Kumar et al., 2012) provides daily surface downward net  
140 heat flux derived using the COARE v3.0 algorithm from a combination of bias-corrected

141 ERA-Interim reanalysis and International Satellite Cloud Climatology Project (ISCCP)  
 142 data. Data are available on a  $1 \times 1^\circ$  grid over the equatorial ocean.

143 Components of 10 m wind used in this study are from the European Centre for Medium  
 144 Range Weather Forecasts (ECMWF) Reanalysis Version 5 (ERA-5) reanalysis (Hersbach  
 145 et al., 2020). Data are supplied on a global  $0.25^\circ \times 0.25^\circ$  resolution grid. Hourly data  
 146 were averaged to daily mean values.

## 147 2.2 Ocean reanalysis dataset

148 We use the NEMO ocean model analysis with data assimilation, specifically the  
 149 operational Mercator global ocean analysis and forecast system (global-analysis-forecast-  
 150 phy-001-024 data set Madec, 2008) daily mean fields on a  $1/12^\circ \times 1/12^\circ$  grid (approx-  
 151 imately 8 km in the tropics), to evaluate the CCKW-associated structures of conserva-  
 152 tive temperature, absolute salinity, sea surface height, and ocean velocity between 2007  
 153 and 2017. The NEMO product has 50 vertical levels (from the surface to 5500 m depth)  
 154 with a vertical grid spacing that increases from 1 m to 14.5 m within the upper 100 m.  
 155 Its atmospheric forcing is taken from the 3-hourly ERA-Interim data set (Dee et al., 2011).  
 156 Conservative temperature ( $T$ ) and absolute salinity ( $S$ ) are derived using the TEOS-10  
 157 toolbox (McDougall & Barker, 2011). The ability to simulate the upper ocean circula-  
 158 tion and salinity structure was assessed for various versions of Nemo model in the Bay  
 159 of Bengal, being the  $1/12^\circ$  resolution the most successful (Benshila et al., 2014).

160 The mixed layer depth (MLD), isothermal layer depth (ILD), barrier layer thick-  
 161 ness (BLT), heat content above the mixed layer (HC), and depth of the  $20^\circ\text{C}$  isotherm  
 162 (D20) were calculated from vertical profiles of  $T$  and  $S$ . Following Sprintall and Tom-  
 163 czak (1992), de Boyer Montégut et al. (2007), and Drushka et al. (2014), the ILD was  
 164 defined as the depth ( $D$ ) at which the temperature falls to a threshold  $\Delta T = 0.3^\circ\text{C}$  be-  
 165 low a reference temperature at 5 m depth  $T_{ref} = T(D = 5)$ :

$$\text{ILD} = D|_{T=T_{ref}-\Delta T}. \quad (1)$$

166 The MLD was then calculated similarly, using  $\Delta\sigma_\theta$  as the potential density change rel-  
 167 ative to the reference density at 5 m,

$$\text{MLD} = D|_{\sigma_\theta=\sigma_\theta(D=5)+\Delta\sigma_\theta}, \quad (2)$$

168 where  $\Delta\sigma_\theta$  is the change in potential density needed to effect a decrease in temperature  
 169 of  $\Delta T$ , assuming salinity is held constant:

$$\Delta\sigma_\theta = \sigma_\theta(T_{ref} - \Delta T, S_{ref}, P_0) - \sigma_\theta(T_{ref}, S_{ref}, P_0). \quad (3)$$

170 Here,  $S_{ref}$  is  $S$  at the reference depth of 5 m and  $P_0$  is pressure at the ocean surface. The  
 171 BLT is defined as

$$\text{BLT} = \text{ILD} - \text{MLD} \quad (4)$$

172 The HC is calculated by integrating the amount of heat above the MLD:

$$\text{HC} = \int_{z=-\text{MLD}}^0 \rho_w c_w T dz, \quad (5)$$

173 where  $z$  is the vertical coordinate (positive upward), and  $\rho_w$  and  $c_w$  are the in situ den-  
 174 sity and specific heat capacity of sea water, respectively.

175 The calculation of the derived variables showed only a small sensitivity to the choice  
 176 of the  $\Delta T$  threshold. Using values of 0.3, 0.4 and 0.5°C for  $\Delta T$  resulted in mean and  
 177 standard deviations of 35.2±3.5 m for ILD, 24.7±3.2 m for MLD, and 10.5±0.3 m for  
 178 BLT in the equatorial Indian Ocean.

### 179 **2.3 Classifying CCKW events**

180 Using precipitation from TRMM and the methodology of Baranowski et al. (2016a),  
 181 a database of CCKW events occurring globally between 2007 and 2017 was generated.  
 182 The approach tracks individual events and provides information of their longitude along  
 183 the equator at 3-hourly time intervals. It utilizes space-time FFT-filtered precipitation  
 184 anomalies associated with the CCKW spectrum (Kiladis et al., 2009) and defines tra-  
 185 jectories as the continuous maxima of CCKW-filtered precipitation exceeding a thresh-  
 186 old value (2.5 mm day<sup>-1</sup> anomaly).

187 The CCKW event dataset was then further subset to isolate events relevant to the  
 188 area of interest. This study focuses on CCKW propagation across the Indian Ocean and  
 189 the Maritime Continent. Hence, a base point longitude was set at 110°E in the western  
 190 Maritime Continent (Fig. 1). All CCKW events considered in this study cross this base  
 191 point longitude. Furthermore, to guarantee a minimum zonal extent of each CCKW event,  
 192 each trajectory considered had to begin west of 90°E and end east of 120°E.

193 These constraints led to a total of 381 such CCKW events active over the eastern  
 194 Indian Ocean and Maritime Continent between 2007 and 2017. These events were fur-

195 ther classified based on their instantaneous precipitation anomaly at the base point ( $110^{\circ}\text{E}$ )  
 196 and on their average precipitation anomaly between  $100 - 120^{\circ}\text{E}$ . The  $N = 82$  events  
 197 whose precipitation anomaly was in the upper quartile (i.e., above  $7.7 \text{ mm day}^{-1}$ ) were  
 198 classified as “strong” events.

199 Within our CCKW subset, 52% of the strong events are preceded or followed by  
 200 another CCKW event within five days. As such a large proportion of CCKW events is  
 201 preceded or followed by another event within a CCKW lifetime span (approximately 4–  
 202 5 days; Baranowski et al., 2016a), a further classification was made to avoid interference  
 203 between events and to allow an analysis of the physical response of the undisturbed ocean  
 204 to the passage of a CCKW. The CCKW events that were not preceded or followed by  
 205 any other event within five days, are termed “solitary” events. The results presented in  
 206 this study are focused on the conditions associated with strong, solitary CCKW events  
 207 ( $N = 36$ ). There is a slight bias in the seasonal distribution of these strong, solitary  
 208 CCKW events, with 22 events occurring in northern summer (April–September), and  
 209 14 in northern winter (October–March).

## 210 **2.4 CCKW composite calculation**

211 To create CCKW composite fields, the annual cycle was first removed from the daily  
 212 time series of all variables of interest, at each grid point and level. Each time series was  
 213 then filtered using a Lanczos 20-day high-pass filter with 241 weights. This filtering al-  
 214 lows the analysis of a “pure” CCKW structure, by removing the signal of any MJO, and  
 215 other atmospheric systems with a longer time scale, that the CCKWs are often embed-  
 216 ded in. These filtered anomaly time series are then used to construct the CCKW com-  
 217 posite fields.

218 A base point at  $110^{\circ}\text{E}$  was chosen for referencing the CCKW events. Thus, the day  
 219 that each event passes through the base point at  $110^{\circ}\text{E}$  is defined as the lag 0 day for  
 220 that event. The lagged composites are then created by averaging the anomaly fields re-  
 221 ferenced these lag 0 days. Daily composite fields from lag  $-10$  days to  $+10$  days were cal-  
 222 culated.

223 Each individual CCKW event will have a slightly different phase speed. Each event  
 224 is referenced to the day it crosses the base point at  $110^{\circ}\text{E}$ . Hence, all the events “con-  
 225 structively” interfere at lag 0 to give a strong signal then. However, as the magnitude

226 of the lag increases (for both positive and negative lags), the events will begin to par-  
 227 tially destructively interfere and the composite signal may be weakened. To test for the  
 228 importance of this and for the choice of base point, we composited daily lags for a range  
 229 of base points (from 50 to 120°E). These zero-lagged composites at different base points  
 230 do not suffer from the destructive interference problem. At each longitudinal base point,  
 231 we compared the lag 0 composite with its respective time-lagged-composite for the re-  
 232 maining longitudinal base points. It transpired that the main features were not sensi-  
 233 tive to the choice of method (composites generated by lagging time and longitudinal base  
 234 points). Hence, unless we take composites created with extreme longitudinal base points  
 235 and time lags, the destructive interference at high lags is not a major problem. Based  
 236 on this comparison, we identified 110°E as the ideal base point that allows following oceanic  
 237 features propagating further east in the domain without having issues with destructive  
 238 interference in the time lags of interest.

239 In addition to showing composite maps on horizontal surfaces, composite vertical  
 240 sections are also shown. To diagnose the anticipated path of an oceanic Kelvin wave forced  
 241 by the atmospheric CCKW over the Indian Ocean, three distinct vertical sections are  
 242 computed, then spliced together end to end (Fig. 1a). The data along the sections were  
 243 averaged over a  $\pm 0.5^\circ$  band in latitude for section A and longitude for sections B and  
 244 C. For sections B and C, which are not meridional, the data are firstly linearly interpo-  
 245 lated onto the section with a grid that maintains the distance between points as observed  
 246 at the Equator (i.e., 9.25 km).

### 247 **3 Mean atmospheric and oceanic background state**

248 The average wind field and oceanic conditions that preceded the strong solitary CCKW  
 249 events are presented in Fig. 2. These fields were computed by compositing the total fields  
 250 between lags  $-10$  and  $-6$  days, and represent the precursor atmospheric and oceanic state  
 251 that the CCKW events develop on. The slight seasonal bias to the distribution of events,  
 252 as discussed in Section 2.3, is reflected in the precursor wind field, which shows a struc-  
 253 ture similar to the boreal summer monsoon (Fig. 2d).

254 The depth of the 20°C isotherm (D20; Fig. 2c) is typically used to represent the  
 255 depth of the mid-thermocline in the tropical ocean, and as an indicator of the ocean dy-  
 256 namic response to wind forcing (Schott et al., 2009). For example, the shallower D20 ob-

257 served off the coast of Java is consistent with the predominantly alongshore winds that  
258 force coastal upwelling processes in this region during northern summer. Cooler surface  
259 waters (Fig. 2a) are then associated with this upwelling.

260 Another climate relevant feature is the barrier layer, a consequence of temperature  
261 and salinity near-surface stratification in areas of high fresh water input. In regions of  
262 high precipitation or river discharge, for example along the Sumatran coast, the light fresh  
263 waters (Fig. 2e) cause a vertical density gradient within the relatively homogeneous tem-  
264 perature surface layer that will act as a “barrier” for surface heat fluxes (Godfrey & Lind-  
265 strom, 1989; Schott et al., 2009). We observe a relatively thick barrier layer along the  
266 Sumatran coast (Fig. 2g), particularly north of the Equator, likely associated with the  
267 high precipitation rates in the region (not shown) and possibly the periodic advection  
268 of fresh plumes exiting the Sunda Strait (Potemra et al., 2016).

269 The temperature and salinity precursor fields are also presented along the sections  
270 A, B and C (Fig. 3a,b) to show the oceanic vertical structure. The composites clearly  
271 show the surface temperature maximum, and the upwelling system off the coast of Suma-  
272 tra (section B) and Java (section C), together with the shallowing of the MLD and ILD  
273 (black and pink dashed lines; Fig. 3a). It also shows the subsurface salinity maximum  
274 (Fig. 3b), which is likely due to the advection by equatorial currents of a high salinity  
275 water mass generated in the Arabian Sea (Masson et al., 2002; Nagura & Mcphaden, 2018;  
276 Prasad & Ikeda, 2002), as well as the low salinity surface waters at the Sumatran coast  
277 and off the Sunda Strait (western and eastern end of section B, respectively). The dis-  
278 tance between the MLD and the ILD indicates the thickness of the barrier layer, which  
279 increases towards the coast (Fig. 3a,b).

#### 280 **4 Atmospheric structure of CCKWs**

281 The atmospheric structure of CCKWs is briefly described here and compared with  
282 previous studies, to provide the context and forcing fields for the oceanic subsurface struc-  
283 ture of the CCKWs that follows in Section 5. The definition of CCKW events used here  
284 is based on eastward-propagating maxima in equatorial precipitation. Hence, as expected,  
285 lagged composite anomalies of precipitation show a coherent positive anomaly over the  
286 central Indian Ocean at lag  $-5$  days (Fig. 1a). This propagates smoothly eastward over  
287 the eastern Indian Ocean by lag  $-3$  days (Fig. 1b) and over the western Maritime Con-

288    continent by lag  $-1$  day (Fig. 1c), reaching the reference longitude of  $110^\circ\text{E}$  at lag 0, by de-  
 289    sign. By lag 1 day (Fig. 1d) the positive precipitation anomaly has reached the central  
 290    Maritime Continent; it then propagates out of the domain shown in Fig. 1 at subsequent  
 291    lags. The phase speed is approximately 10 degrees longitude per day ( $13 \text{ m s}^{-1}$ ), con-  
 292    sistent with previous observations of CCKWs (e.g., Wheeler & Kiladis, 1999; Roundy,  
 293    2008; Baranowski et al., 2016a).

294        The anomalous surface wind stress vectors also show a signal consistent with the  
 295    known structure of atmospheric CCKWs (Wheeler et al., 2000). An eastward-propagating  
 296    patch of eastward wind stress anomalies on the equator accompanies the positive pre-  
 297    cipitation anomalies and enhanced convection there from lag  $-3$  to  $-1$  days (Fig. 1j,k).

298        The increase in cloudiness associated with the positive precipitation anomalies will  
 299    lead to a decrease in surface shortwave radiation flux during the convectively active phase  
 300    of the CCKWs. The westerly winds associated with the eastward surface wind stress anoma-  
 301    lies will add to the mean westerly winds over the equatorial Indian Ocean, increasing sur-  
 302    face evaporation and decreasing the (downward) surface latent heat flux into the ocean.  
 303    Both these flux anomalies lead to an upward net heat flux anomaly of over  $20 \text{ W m}^{-2}$   
 304    into the ocean from lag  $-3$  to  $-1$  days (line contours showing negative NHFD anoma-  
 305    lies in Fig. 1b,c).

306        In addition to the canonical eastward propagation along the equator, the CCKWs  
 307    also exhibit northward and southward propagation when they reach the island of Suma-  
 308    tra. The Barisan mountain range runs along the western coast of Sumatra and consis-  
 309    tently reaches altitudes of 2000 m, well above the height of the atmospheric boundary  
 310    layer, and forms a partial topographic barrier to the eastward propagation. Note that  
 311    Sumatra and the mountain range run along a northwest–southeast axis, rather than a  
 312    north–south axis. The convective component of the CCKWs responds to this inclined  
 313    barrier, with a northward and southward extension of the convective anomalies over the  
 314    eastern Indian Ocean off the coast of Sumatra at lag  $-1$  day (Fig. 1c).

315        The dynamical component of the CCKWs also responds, with a stronger response  
 316    to the south, as the eastward wind stress anomalies along the equator become southeast-  
 317    ward anomalies running parallel to the Sumatran coast and mountain range (Fig. 1k).  
 318    This response can be interpreted as the atmospheric equivalent to a coastal Kelvin wave  
 319    (e.g. Webber et al., 2012), trapped against the topographic barrier of the Barisan moun-

320 tains. An equivalent atmospheric topographically trapped Kelvin wave has previously  
 321 been noted, when the atmospheric equatorial Kelvin wave component of the MJO im-  
 322 pinges on the Andes mountain range, after traversing the Pacific Ocean (Matthews, 2000).

## 323 5 Subsurface oceanic structure of CCKWs

### 324 5.1 Immediate ocean response

#### 325 5.1.1 Thermodynamic response

326 The SST over the eastern Indian Ocean and Maritime Continent generally shows  
 327 a decrease during the passage of the CCKW, with negative SST anomalies appearing over  
 328 the central equatorial Indian Ocean at  $80^{\circ}\text{E}$  at lag  $-3$  days (Fig. 4b), then moving east-  
 329 ward across the domain to the eastern Indian Ocean at lag  $-1$  day (Fig. 4c) and the west-  
 330 ern Maritime Continent by lag 1 day (Fig. 4d).

331 The evolution in time of the upper ocean daily temperature anomalies averaged  
 332 at the Equator between  $90^{\circ}\text{E}$ - $95^{\circ}\text{E}$  shows the local effect of the passage of CCKW events  
 333 in the SST (surface temperature in Fig. 5d). We estimate that this area experiences a  
 334 decrease in temperature of  $0.19^{\circ}\text{C}$  between the maximum temperature anomaly observed  
 335 2 days before the CCKW passage by this longitudinal band (lag  $-4$  day) to its mini-  
 336 mum anomalies the day following the event (lag  $-1$ ; Fig. 5d). This is consistent with  
 337 previous results from Baranowski et al. (2016a). The agreement in timing and magni-  
 338 tude of the SST anomalies between this study and the estimate of Baranowski et al. (2016a)  
 339 validates the use of NEMO data in analysing the oceanic response to CCKWs. We then  
 340 use the multi-level nature of the NEMO data to extend the analysis below the surface.

341 The surface temperature signal extends downward in the equatorial eastern Indian  
 342 Ocean (section A, lags  $-1$  to 3 days, colour shading in Fig. 6a) through the mixed layer  
 343 (MLD shown by black lines in Fig. 6a). The temperature signal becomes weaker with  
 344 depth and lagged in time within the mixed layer. For example, at 25 m (average MLD  
 345 at  $90^{\circ}\text{E}$  in the precursor field; Fig. 3), the minimum temperature anomaly ( $-0.03^{\circ}\text{C}$ ;  
 346 35% of surface minimum) is observed at lag 0, a day later than at the surface and two  
 347 days after the peak CCKW precipitation anomaly at  $90^{\circ}\text{E}$  (Figs. 5d,h).

348 The surface cooling is consistent with the observed decrease in downward net heat  
 349 flux (NHFD; line contours in Fig. 1a-d). This in turn is due to a combination of a de-

350 crease in incoming solar radiation (inferred from the positive precipitation anomalies,  
 351 and therefore increased cloudiness (colour shading in Fig. 1a–d), and strong westerly wind  
 352 anomalies (Fig. 1j,k) increasing the upward latent heat flux.

353 Stronger winds associated with the passage of the CCKWs can also contribute to  
 354 the cooling of surface waters by reducing vertical stratification through vertical mixing  
 355 (Fig 5d, e.g., negative anomalies in  $N^2$  at waters above MLD coincident with positive  
 356 anomalies in wind at lag  $-2$  at Fig. Fig 5f). The local change in stratification during  
 357 the passage of CCKWs can be observed in the anomalies averaged over the Equator ( $2.5^\circ\text{N}$ -  
 358  $2.5^\circ\text{S}$ ,  $90^\circ\text{E}$ - $95^\circ\text{E}$ ; Figs. 5e).

359 While changes in  $N^2$  (Figs. 5e) appear to be mostly aligned with temperature anoma-  
 360 lies (Fig. 5d), salinity also contributes to it, mainly in the initial lags of enhanced pre-  
 361 cipitation (Fig. 5i). Between lags  $-4$  to  $-3$ , when precipitation anomalies start to increase  
 362 (Fig. 5i),  $N^2$  anomalies are high (Fig. 5e) due to this input of fresh water and high sur-  
 363 face temperatures (Fig. 5d). With the decrease in NHFD (Fig. 5a) and the increase in  
 364 wind stress (Fig. 5f), temperature drops at the surface, leading to a reduction in  $N^2$  de-  
 365 spite the continuous decrease in salinity (Lags  $-3$  to  $-2$ ). The wind-driven vertical mix-  
 366 ing then acts on further reducing vertical stratification, deepening the MLD and con-  
 367 tributing to the spreading of the negative temperature and salinity anomalies with depth  
 368 (Figs. 5d,i).

369 Moreover, the stronger eastward wind anomalies at the Equator (Figs. 1j,k and 5f)  
 370 intensify the eastward surface currents, as shown by the positive anomalies in the sur-  
 371 face zonal currents between lags  $-1$  and  $0$  (Fig. 7a). This intensification of surface cur-  
 372 rents and the momentum transference with depth (Fig. 7a) likely increases vertical shear  
 373 and contributes to generation of turbulence (Moum et al., 2014; Pujiana & McPhaden,  
 374 2018).

375 The role of subsurface turbulence in modulating the upper ocean temperature dur-  
 376 ing CCKW events is supported by Pujiana and McPhaden (2018), who showed that, be-  
 377 tween 2011 and 2012, surface heat flux and subsurface turbulent heat fluxes had simi-  
 378 lar contributions to the surface layer cooling in this region (at  $0^\circ\text{N}$ ,  $90^\circ\text{E}$ ). Thus, the sub-  
 379 surface turbulent heat fluxes can be an important contributor to maintaining the cool-  
 380 ing of the mixed layer observed up to 8 days after the passage of CCKW events (e.g. lag  
 381  $+6$  days in Fig. 5d). The changes in stratification observed in this study using the NEMO

382 data are consistent with the in situ work of Pujiana and McPhaden (2018), and serve  
 383 to spatially extend their conclusions across the Indian Ocean basin.

384 The heat content of the mixed layer is a key variable that impacts atmospheric con-  
 385 vection within the CCKW and subsequent feedbacks, as it represents the reservoir of heat  
 386 that is available to the atmosphere. The heat content (HC: Equation 5) is dependent on  
 387 both the temperature and depth of the mixed layer. Despite the existence of negative  
 388 temperature anomalies within the mixed layer, anomalies in HC closely follow anoma-  
 389 lies in the MLD (Fig. 5b,d). Thus, most of the increase in HC observed along the Equa-  
 390 tor between lags  $-2$  days and 0 days is likely due to deepening of MLD mostly from wind  
 391 mixing (Figs. 5 and 4).

392 The precipitation (Fig. 5h) and wind stress (Fig. 5f) forcings for the CCKW are  
 393 relatively short lived; they last 4 days, from lag  $-4$  to 0 in the equatorial eastern Indian  
 394 Ocean ( $2.5^{\circ}\text{S}$ – $2.5^{\circ}\text{N}$ ,  $90$ – $95^{\circ}\text{E}$ ). However, the ocean response is longer lived. For exam-  
 395 ple, the negative ocean temperature anomalies (Fig. 5d) last 6 days at the surface (lag  
 396  $-2$  to 4) and 7 days at 20–40 m (lag  $-1$  to 6). The increase in MLD (Fig. 5d) is also rel-  
 397 atively long lived. This is reflected in the positive heat content anomalies (Fig. 5b), which  
 398 last 6 days, from lag  $-1$  to 5. These results are consistent with Baranowski et al. (2016a),  
 399 who hypothesized a long-lasting effect of the CCKWs based on the ocean surface response  
 400 up to 5 days after the events.

### 401 **5.1.2 Dynamical response**

402 The ocean will also respond dynamically to the easterly wind anomalies along the  
 403 equator at lag  $-5$  days (Fig. 1i). This is evidenced by the negative anomalies in SSH  
 404 and in D20 (indicating shallower depths) in this region two days after the forcing (lag  
 405  $-3$  days; Fig. 4j), indicating oceanic upwelling. Similarly, the intensification of south-  
 406 easterly winds along the Sumatran coast at lag  $-5$  days (Fig. 1i) induces coastal upwelling  
 407 two days later (lag  $-3$  days; Fig. 4j) due to Ekman transport. The coastal upwelling sig-  
 408 nal persists at the Sumatran coast until lag 0.

409 Temperature anomalies in the ocean interior are consistent with the upwelling of  
 410 deeper, colder waters; negative anomalies in D20 (black line in Fig. 6a) coincide with  
 411 negative temperature anomalies below 70 m (Fig. 6a; lag  $-3$ ). Because the coastal re-  
 412 gion is characterised by shallower MLD and a subsurface salinity maximum (Fig. 3b),

413 this coastal upwelling is likely to be the cause of the positive salinity anomalies below  
 414 the MLD (Fig. 6b; lag  $-3$ ).

415 Coastal upwelling along the southwestern coasts of Sumatra and Java is known to  
 416 be associated with prevailing southeasterly winds during the boreal summer monsoon  
 417 (e.g. Wyrski, 1962; Bray et al., 1996; Susanto et al., 2001). Even though the upwelling  
 418 primarily develops between June and September (e.g., Susanto et al., 2001), intrasea-  
 419 sonal variations in the upwelling signal are correlated with intraseasonal variations in  
 420 winds (20–50 day periods) in both summer and winter monsoons along the Java coast  
 421 (Horii et al., 2016). This suggests, together with our composite analysis, that the anoma-  
 422 lies in the wind field associated with the development of CCKW events may be associ-  
 423 ated with the variability in the upwelling system at the Java coast year round, and this  
 424 relation may be stronger during boreal summer when the average atmospheric conditions  
 425 are more favorable for the upwelling to occur and the strong solitary events are more fre-  
 426 quent.

427 The anomalies observed in D20 associated with upwelling ( $\sim 1.5$  m; Fig. 4j-k and  
 428 6a, lags  $-5$  to  $-3$ ) are likely relevant at the Sumatran coast. For example, Horii et al.  
 429 (2016) showed that upwelling events occurring between April-August were associated with  
 430 SST cooling along the Java coast, which can then impact on local atmospheric convec-  
 431 tion. Complementary to their results, we find a similar association at the coast of Suma-  
 432 tra (Fig. 6a, lags  $-5$  to  $-3$ ). This highlights the impact that CCKW events may have  
 433 remotely through anomalies in the wind field and their effect on the ocean dynamics.

434 Similarly, westerly wind stress anomalies during the CCKW passage will also trig-  
 435 ger an immediate oceanic dynamic response. Following the equatorial westerly wind stress  
 436 intensification (lag  $-3$  days; Fig. 1j), downwelling initiates at lag  $-1$  day (positive D20  
 437 and sea surface height anomalies along the Equator between  $82-90^\circ$  E; Fig. 4l) as a con-  
 438 sequence of Ekman convergence at the Equator. This becomes a more coherent signal  
 439 at later lags.

440 The daily anomalies averaged over the equatorial eastern Indian Ocean ( $2.5^\circ$ N– $2.5^\circ$ S,  
 441  $90^\circ$ E– $95^\circ$ E; Fig. 5) show more specifically the evolution of the oceanic state in relation  
 442 to the forcing. While the local westerly wind stress and precipitation anomalies peak at  
 443 lag  $-2$  days with the passage of the CCKW by  $90^\circ$ E (Figs. 5f,h), D20 and ILD anoma-

444 lies in the region reach their maximum 3 days later (lag +1 day; Figs. 5g and gray full  
 445 line in Fig. 5d, respectively).

446 Dynamical changes in the ILD and variations in the MLD by mixing may have an  
 447 effect on the BL thickness. A thick barrier layer can reduce the effect of surface forcing  
 448 in the ocean surface temperature as it potentially inhibits downward turbulent heat flux  
 449 and thus reduce cooling by entrainment (Drushka et al., 2014; Pujiana & McPhaden, 2018).  
 450 We found only small ( $\pm 1$  m) local anomalies in BL thickness during the passage of strong  
 451 solitary CCKW events (Fig. 5c), despite much larger variations in the MLD and ILD  
 452 (black and grey lines, respectively, in Fig.5d). Anomalies in BL thickness of similar mag-  
 453 nitude ( $<2.5$  m) are found across the domain (not shown), being typically larger at the  
 454 Equator. However, there is no coherent spatial pattern to these BL anomalies.

455 These small changes in BL thickness occur because the MLD and ILD anomalies  
 456 tend to co-vary in phase (Fig. 5d). Similarly, Drushka et al. (2014) found weak ( $< 5$  m  
 457 peak-to-peak) anomalies in the BL in the eastern equatorial Indian Ocean during MJO  
 458 events, which were also associated with co-variance between MLD and ILD. Their study  
 459 argued that these small variations are likely results of noise from other subseasonal pro-  
 460 cesses and due to the diversity of the MJO-related atmospheric forcing. However, using  
 461 this rationale, we would expect a more coherent and stronger signal in our results, as we  
 462 use a more selective approach in terms of atmospheric forcing time scales and intensity  
 463 for the CCKWs. Thus, a diversity in the forcing is unlikely to be the cause of the ob-  
 464 served low BL variations.

465 In contrast, Pujiana and McPhaden (2018) reported variation in the BL thickness  
 466 from 10–15 m to 20–30 m during the CCKW life cycle at 90°E, 0°N. Such large anoma-  
 467 lies in BL thickness were argued to be a result of a strengthened salinity stratification  
 468 by rainfall (Pujiana & McPhaden, 2018). Even though the criteria we used to select CCKW  
 469 events has a different principle to those used by Pujiana and McPhaden (2018), they are  
 470 aimed to isolate events of consistently strong precipitation through the wave’s trajec-  
 471 tory. Thus, it was expected that we would find similarly high BL anomalies, which was  
 472 not observed.

473 As precipitation is unlikely the cause for the discrepancy in the BL response be-  
 474 tween these studies, this must be related to differences in the strength of the wind anoma-  
 475 lies and/or in the oceanic precursor stratification. Thus, even though the relatively thick

476 BL will act to buffer the mixed layer from the deeper ocean, the small variations observed  
 477 in the BL thickness (Fig. 5d) throughout the CCKW passage suggest a weak role of the  
 478 BL in modulating the inhibition of downward turbulent heat flux. As a caveat, we should  
 479 also consider the possibility that the discrepancy in the barrier layer thickness behav-  
 480 ior between models and observations (e.g., Pujiana & McPhaden, 2018) could be related  
 481 to shortcomings of the reanalysis, as for example, an overly strong vertical mixing that  
 482 could quickly erode the BL and be the cause of the small changes in BL thickness.

## 483 5.2 Delayed ocean response and remote effects

484 In addition to the immediate response described in Section 5.1, the passage of CCKW  
 485 events will also trigger dynamical processes on longer, oceanic time scales.

486 We observe the eastward propagation of the downwelling anomalies that followed  
 487 the westerly wind stress anomalies associated with the CCKW passage. At lag 0, the pos-  
 488 itive anomalies in D20 and SSH are mostly constrained along the equatorial band (ex-  
 489 tending from roughly between 82°E–90°E; not shown), indicating local downwelling with  
 490 change in the D20 of up to 1 m. These anomalies travel eastward and reach the coast  
 491 of Sumatra at lag +1 days, when it has developed into a coherent downwelling signal oc-  
 492 cupping a broad longitudinal range along the Equator ( $\sim 75 - 99^\circ$  E; Fig. 4l). These  
 493 eastward moving positive anomalies in D20 and SSH suggest the propagation of a down-  
 494 welling oceanic Kelvin wave (OKW), initially triggered by the westerly wind burst as-  
 495 sociated with the atmospheric CCKW.

496 The propagation along the Equator of the suggested downwelling Kelvin wave sig-  
 497 nal can also be identified by the coherent positive temperature anomalies just below the  
 498 ILD (solid magenta line in Fig. 6a). These anomalies in subsurface temperature are co-  
 499 incident with positive D20 and SSH anomalies and intensification of subsurface zonal cur-  
 500 rents (averaged between 60-200 m; Fig. 6a). Because the region is characterised by a pos-  
 501 itive vertical temperature gradient (Fig. 3a), these positive temperature anomalies are  
 502 caused by the downwelling isothermals associated with the propagation of the oceanic  
 503 wave and demonstrate the capacity of the atmospheric forcing in affecting the deeper  
 504 ocean.

505 While the subsurface temperature anomalies associated with the oceanic wave be-  
 506 come stronger and more coherent as it propagates along the Equator (lags  $-1$  to  $1$ ; Fig.

507 **6a**), when the wave reaches the Sumatran coast, part of the signal is lost and part of it  
 508 propagates southeastward as a coastal Kelvin wave along the coast of Sumatra and Java  
 509 (**Figs. 6**). The maximum anomalies in temperature, SSH and D20 becomes weaker as  
 510 the wave propagates along the Sumatra and Java coast (lags 3 to 9; **Figs. 6**), suggest-  
 511 ing energy dissipation possibly by interaction with the topography or by reflecting as Rossby  
 512 waves, as observed by Webber et al. (2010) and Pujiana and McPhaden (2020). The south-  
 513 easterly wind anomalies along the coast (lag 7; **Fig. 1**), which can shoal the thermocline  
 514 via Ekman transport, could also potentially contribute to the weakening of the down-  
 515 welling Kelvin wave and its signal in SSH and D20 anomalies.

516 Although the propagation of the oceanic wave is not easily identifiable in salinity  
 517 anomalies along the section (**Fig. 6b**), the local variation in the salinity anomalies at the  
 518 Equator (**Fig. 5i**) show changes in agreement with the passage of the oceanic wave (i.e.,  
 519 negative salinity anomalies during downwelling), with lowest anomalies at lag +1 days  
 520 when MLD is deepest). These negative anomalies are expected as the background ver-  
 521 tical salinity gradient in the region is negative, i.e., salinity increases with depth (**Fig.**  
 522 **3b**).

523 The highest anomalies of temperature and salinity are observed at lag +1 just be-  
 524 low the ILD (**Fig. 6a**) and MLD (**Fig. 5i**), respectively. As the wave propagates eastward,  
 525 these anomalies extend down to 200 m for temperature, while salinity anomalies are mostly  
 526 restricted to the top 110 m (**Figs. 6a-b**). This difference is likely due to the background  
 527 vertical gradient, which becomes relatively weak below 110 m for the salinity field, but  
 528 remains positive for temperature up to greater depths (**Fig. 3a-b**).

529 To better assess the depth-response of the ocean to the passage of CCKWs we eval-  
 530 uate the vertical structure of the oceanic Kelvin wave by analysing the composite of zonal  
 531 velocity anomalies in the top 180 m (**Fig. 7a**). Near the surface, zonal currents show strong  
 532 positive anomalies peaking at lag 0. The roughly uniform phase with depth observed mostly  
 533 above 40 m coincides with the mixed layer and indicates the immediate response to wind  
 534 forcing. At the MLD, there is an abrupt change of phase, with the zonal current anoma-  
 535 lies peaking at lag 4 days immediately below the ML. Below this depth, current anoma-  
 536 lies show a gradual vertical shift in phase, with deeper levels tending to lead shallower  
 537 levels. A more pronounced phase shift is observed below 100 m, in agreement with the  
 538 structure of a Kelvin wave forced at the surface which, as suggested by linear wave the-

539 ory, would propagate phase upward and energy downward into the ocean interior (McCreary,  
540 Jr., 1984; Iskandar & McPhaden, 2011).

541 From the time the oceanic wave reaches the Sumatran coast (lag +1 days; three  
542 days after the passage of CCKWs by 90°E, Figs. 4l and 6a), it takes on average 3 days  
543 for it to travel along the coast and reach the Sunda Strait (lag +4 days, Fig. 4m), through  
544 which part of the signal seems to propagate within the Java Sea and Karimata Strait  
545 (lag +5 days, positive anomalies in SSH, Fig. 4n). It takes on average 11 days after the  
546 passage of CCKWs by 90°E for the signal of the oceanic Kelvin wave present in the SSH,  
547 D20 subsurface temperature and zonal current anomalies to leave the Sumatran coast  
548 and be restricted to the coast of Java (lag +9 days, Fig. 4p). This roughly corresponds  
549 to 9 days travel since the Kelvin wave signal was identified at 90° E.

550 To evaluate the wave horizontal speeds observed in the anomalies, we compare the  
551 meridional structure of the zonal velocity anomalies (averaged between 100–200 m at 90°E;  
552 Fig. 7b) with Kelvin wave theory. For this analysis we used a 90-day high-pass filter to  
553 take into consideration the longer time scales associated with oceanic response, observed  
554 for example by a “red shift” in the spectrum of the ocean response to intraseasonal at-  
555 mospheric forcing (e.g., Han, 2005; Iskandar & McPhaden, 2011; Nagura & McPhaden,  
556 2012). In this analysis we exceptionally constructed the velocity anomaly composites us-  
557 ing a base point at (90°E). As the aim of this analysis is to investigate the initiation of  
558 the dynamic response, the choice of a base point closer to the region where the oceanic  
559 waves are excited intends to reduce signal interference due to different wave speeds of  
560 propagation. The magnitude of the depth-averaged zonal velocity anomalies at lag +3  
561 days (in this case, 5 days after the passage of the CCKW event) approximates to a Gaus-  
562 sian distribution in latitude within 4°S–4°N (red circles in Fig. 7b), in agreement with  
563 the meridional structure of a Kelvin wave.

564 The depth-averaged composite zonal velocity  $u'(y)$  was least-squares fitted to the  
565 theoretical Kelvin wave solution on an equatorial  $\beta$  plane (Fig. 7b) :

$$u'(y) = u_0 e^{-\beta y^2/2c}, \quad (6)$$

566 where  $\beta = 2.3 \times 10^{-11} \text{ m}^{-1} \text{ s}^{-1}$  is the specified northward gradient of planetary vor-  
567 ticity at the Equator,  $y$  is distance (in m) northward from the equator, and the free pa-  
568 rameters are  $u_0$  amplitude of the wave and  $c$  (the wave phase speed). The best fit val-  
569 ues are  $u_0 = 0.034 \text{ m s}^{-1}$  and  $c = 0.48 \text{ m s}^{-1}$  (blue line in Fig. 7b), which gives an equa-

570 torial trapping scale  $L = \sqrt{2c/\beta}$  of 290 km. The estimated phase speed is close to the  
 571 Kelvin wave theoretical phase speed of the fifth vertical baroclinic mode, which is ap-  
 572 proximately  $0.6 \text{ m s}^{-1}$  (Moore & McCreary, 1990). The vertical structure of the fifth mode  
 573 has crossing points (zero anomaly) at approximately 50 and 150 m depths (Webber et  
 574 al., 2014). This matches the observed structure of the ocean response to the CCKWs  
 575 here, as there are crossing points in the zonal current profile at lag 0 at 50 and 130 m  
 576 (Fig. 7a).

577 The theoretical phase velocity extracted from the data does not match perfectly  
 578 to the theoretical phase velocity of a single projected mode. Such match should not be  
 579 expected as, unless the ocean signal is isolated to depict a specific oscillation, it includes  
 580 the main excited mode (in this case, the fifth) and the contribution from other multi-  
 581 ple vertical modes. This is because the CCKW wind forcing will project onto a number  
 582 of modes, and processes such as constructive interference between wind-forced internal  
 583 waves and Rossby wave reflection at the eastern boundary can mix energy between modes  
 584 (Nagura & McPhaden, 2012).

585 Several studies have highlighted the relationship between the intraseasonal wind  
 586 forcing (e.g. MJO) and an oceanic response dominated mainly by the first two baroclinic  
 587 modes (e.g. Han, 2005; Iskandar et al., 2005; Halkides et al., 2015; Pujiana & McPhaden,  
 588 2020). In contrast, we show that the oceanic response to CCKWs is dominated primar-  
 589 ily by a higher (fifth) baroclinic mode when considering oscillations with periods shorter  
 590 than 90 days. This difference in the main mode excited by the different forcings may be  
 591 one of the factors contributing to the CCKW related anomalies in SSH (0.3-0.6 cm; Fig.  
 592 4i-p) being considerably smaller than anomalies associated with the MJO (e.g. 15- 20 cm;  
 593 Matthews et al., 2010), as its primarily the first modes that make significant contribu-  
 594 tions to the sea level signal (Cane, 1984).

595 Based on common features identified in Hovmöller diagrams of composite anoma-  
 596 lies of zonal velocity (averaged between 100–200 m), D20 and heat content of the mixed  
 597 layer (Fig. 8), the observed signal speeds along the Equator and coasts of Sumatra and  
 598 Java are calculated. Black lines in Fig. 8a are positioned at the center of positive veloc-  
 599 ity anomalies; the different slopes indicate that the signal speed is not uniform along its  
 600 pathway. As the oceanic signal propagates along the Equator (section A; lags  $-2$  to  $3$ ),  
 601 there is still a component of the atmospheric forcing moving eastward at  $\sim 10 \text{ m s}^{-1}$  (with

602 speed much higher than any oceanic mode phase speed) and forcing the ocean, leading  
 603 to a forced oceanic signal that propagates at relatively high speed (on average  $3.2 \text{ m s}^{-1}$ ).  
 604 On reaching the coast, the signal loses energy and stalls, decreasing its average speed to  
 605  $1.9 \text{ m s}^{-1}$  and  $2.0 \text{ m s}^{-1}$  while propagating along the coast of Sumatra and Java, respec-  
 606 tively. The average speed along the entire pathway is  $2.3 \text{ m s}^{-1}$ .

607 The observed average speeds are higher than the estimated theoretical wave speed  
 608 at the Equator. The difference between these two estimates is expected, as the latter ad-  
 609 dresses the generation of the oceanic signal, being an estimate of the main mode excited  
 610 instantaneously by the forcing with the least possible interference. However, the former  
 611 represents the velocity with which the signal effectively propagates through the domain,  
 612 which will result from a combination of the main excited modes, the selective dissipa-  
 613 tion of the modes, the constructive interference between propagating signals in the ocean,  
 614 and the presence of the time-dependent forcing during the propagation of the oceanic  
 615 signal.

616 The variability of OKW phase speeds along their trajectories, and between Kelvin  
 617 wave events, was analysed by Drushka et al. (2010), who estimated phase speeds in the  
 618 range  $1.6\text{--}6.1 \text{ m s}^{-1}$  (average of  $2.6 \pm 1 \text{ m s}^{-1}$ ) for waves crossing the equatorial Indian  
 619 Ocean and along the coast of Sumatra, using 30–90-day filtered altimetric sea level anoma-  
 620 lies. This is further evidence of a spread of OKW speeds along their trajectories, and  
 621 is in agreement with the range of values estimated in this study. Using in situ data and  
 622 satellite altimetry, Iskandar et al. (2005) estimated phase speeds of OKWs associated  
 623 with intraseasonal atmospheric forcing ranging between  $1.5\text{--}2.9 \text{ m s}^{-1}$  along the coast  
 624 of Sumatra and Java. Further southeast, Syamsudin et al. (2004) estimated phase speeds  
 625 between  $1\text{--}3 \text{ m s}^{-1}$  for OKWs entering Lombok Strait ( $8^\circ 46' \text{ S}$ ;  $115^\circ 44' \text{ E}$ ). These es-  
 626 timates are all consistent with our findings for the OKW speeds along the coast of Suma-  
 627 tra ( $1.9 \text{ m s}^{-1}$ ) and Java ( $2.0 \text{ m s}^{-1}$ ), associated with CCKW forcing.

628 In contrast to previous studies which actively selected or filtered general Kelvin waves  
 629 in the ocean (e.g. Syamsudin et al., 2004; Drushka et al., 2010; Iskandar et al., 2005; Pu-  
 630 jiana & McPhaden, 2020), this study focuses on interpreting a wave signature that arises  
 631 consistently in the ocean as a response to specific atmospheric forcing events, i.e., strong  
 632 solitary CCKWs. Consequently, differences in the estimated wave properties, such as the  
 633 dominant baroclinic mode and the wave speed, may be expected. However, the major

634 features identified in the vertical and meridional structures of the oceanic anomalies are  
 635 consistent with previous studies. Moreover, the wave-like signal is not sensitive to the  
 636 choice of a base point, showing consistency in the generation of this oceanic feature. These  
 637 results thus indicate that the passage of CCKWs is an important source for generation  
 638 of oceanic Kelvin waves in the eastern Indian ocean.

## 639 **6 Oceanic feedback**

640 Deepening of the thermocline associated with propagation of oceanic Rossby waves,  
 641 and subsequent increase in SST due to reduced entrainment of subsurface cold waters,  
 642 leads to changes in surface heat fluxes that can subsequently feed back into MJO devel-  
 643 opment (Webber et al., 2012). In a similar way, the deepening of the MLD and conse-  
 644 quent increase in HC observed with the passage of CCKW events (Fig. 4s-v) can feed-  
 645 back onto the atmosphere by modulating atmospheric boundary layer temperature (Baranowski  
 646 et al., 2016a), and potentially contribute to the development of following CCKW events  
 647 or even processes with time scales different from the initial forcing.

648 To evaluate the net effect of the passage of strong solitary CCKW events through  
 649 the study area, the increase in heat content within the ML (in the box 8°S–4°N, 75–100°E),  
 650 from before the passage of the CCKW event (lags –10 to –6 days), to after the passage  
 651 (lags 0 to 4 days) is estimated to be  $1.52 \times 10^8 \text{ J m}^{-2}$  (Fig. 5j). These domain-averaged  
 652 HC anomalies (Fig. 5j) due to solitary strong events remain positive for 6 days, longer  
 653 than the CCKW time-span, similar to that observed for the local anomalies at the Equa-  
 654 tor (Fig. 5b).

655 The domain-averaged increase in the HC includes both the immediate increase in  
 656 HC associated with deepening of MLD by wind mixing during the passage of the CCKW  
 657 (Fig. 5b), and the remote effects of the CCKW on the HC by the propagation of the oceanic  
 658 wave Figs. 8b and 4u,v). For example, at lag +5 days (Fig. 4v), the remote oceanic re-  
 659 sponse to the atmospheric forcing, generated initially in the equatorial band, can be iden-  
 660 tified by the increase in HC related to a deeper MLD off the coast of Sumatra. This in-  
 661 crease in HC can then interact with atmospheric processes such as the diurnal precip-  
 662 itation cycle, and can even influence local flooding (Baranowski et al., 2016b, 2020). Thus,  
 663 the oceanic feedback from the passage of CCKWs can occur away from the forcing re-  
 664 gion and influence processes with time scales different from the initial forcing.

## 7 Conclusions

This study uses a variety of atmospheric datasets and the oceanic NEMO analysis to build a three-dimensional view of the oceanic response to the passage of CCKWs through the eastern equatorial Indian Ocean between 2007 and 2017. The analysis is focused on the robust oceanic response to isolated (“solitary”) strong forcing events, aiming at a better understanding of the physical processes without interference between CCKW events.

Using a statistical approach based on daily composite anomalies, our results show an immediate local thermodynamic and dynamic oceanic response to the passage of the CCKW through the eastern Indian ocean. As downward net heat flux decreases, and eastward winds and currents intensify, vertical shear is likely enhanced by momentum transfer from the atmosphere to the ocean, leading to surface and upper ocean cooling, and a consequent decrease in vertical stratification. As the mixed layer deepens, there is an increase of the mixed layer heat content. These local effects in the ocean surface and interior are shown to last for longer than the local atmospheric forcing. For example, the increase in the mixed layer heat content lasts for six days after the passage of the CCKW, which may then feed back into the atmospheric boundary layer, supporting suggestions from previous studies that CCKWs have a rectifying effect.

Anomalies observed in the wind field related to strong CCKW events are shown to be associated with variability in the upwelling system along the coast of Sumatra and Java, as a dynamical response to the atmospheric forcing. These coastal upwelling events could have a local impact on atmospheric convection by modulating SST (Horii et al., 2016) and also on biological productivity off the Sumatran coast by modifying near-surface nutrient availability Iskandar et al. (2009).

The passage of CCKWs also triggers a consistent oceanic dynamic response on longer time scales. The initial downwelling observed at the Equator associated with the atmospheric forcing develops into a signal identified as a downwelling oceanic Kelvin wave. The propagation of this wave signal is identified in the ocean surface and interior up to 11 days after the passage of the CCKW. The structure of the oceanic signal is consistent with wave theory and shows that, in contrast to the typical response to intraseasonal wind forcing (e.g., Iskandar et al., 2005; Halkides et al., 2015; Pujiana & McPhaden, 2020), CCKWs primarily excite higher oceanic Kelvin wave baroclinic modes. The ob-

697 served oceanic wave signal propagates along the eastern equatorial Indian ocean to the  
698 coast of Java carrying energy into the ocean interior, with an average horizontal speed  
699 ( $2.3 \text{ m s}^{-1}$ ) consistent with observational studies. These results indicate that CCKWs  
700 are an important source for generation of Kelvin waves in the eastern Indian Ocean and  
701 highlight their impact on oceanic conditions away from their main equatorial pathway.

702 Among the CCKW remote effects is the increase in HC due to MLD deepening ob-  
703 served along the Sumatran coast up to 7 days after the peak in the forcing at the Equa-  
704 tor. Hence, the oceanic feedback to the forcing may occur in remote areas, and possi-  
705 bly influence processes of different time scales, such as daily precipitation cycles, or in-  
706 tensify the conditions for flooding in the nearby populated areas.

707 Within the study period, the number of solitary CCKW events, on which we fo-  
708 cus our study, provide a clear statistical representation of the processes associated with  
709 this atmospheric weather system. However, they do not represent the majority of events;  
710 CCKW events are frequently followed by another CCKW event within their life cycle.  
711 In this scenario, the existence of a second peak in the atmospheric forcing would pro-  
712 duce an effect in the ocean that could interact with the first signal, and potentially lead  
713 to higher amplitude and longer lasting anomalies. Further investigation is required to  
714 understand which factors are most important in defining the development of such sequen-  
715 tial CCKWs, and how these feedback onto the system. Finally, the understanding of the  
716 processes involved in the response to isolated forcing is important not only to feedback  
717 into forecast models, but also to further comprehend the interaction of these responses  
718 with forcing of similar or multi-time scales.

## 719 **Acknowledgments**

720 This work was part of the Equatorial Line Observations project, funded by the UK Nat-  
721 ural Environment Research Council (NERC; grant NE/R012431/1) and the US National  
722 Science Foundation (NSF; grant 1724741), and the TerraMaris project (grant NE/R016704/1).  
723 D.B.B. has been supported by the Foundation for Polish Science (The Multi-scale in-  
724 teractions over the Maritime Continent and their role in weather extremes over Central  
725 and Eastern Europe project is carried out within the Operational Programme Smart Growth  
726 2014-2020, Measure 4.4: Increasing the human potential in R&D sector, HOMING pro-  
727 gramme of the Foundation for Polish Science co-financed by the European Union under  
728 the European Regional Development Fund). The TRMM 3B42 data were downloaded

729 from NASA/Goddard Space Flight Center ([https://disc.gsfc.nasa.gov/datasets/](https://disc.gsfc.nasa.gov/datasets/TRMM_3B42_Daily_7/summary)  
730 [TRMM\\_3B42\\_Daily\\_7/summary](https://disc.gsfc.nasa.gov/datasets/TRMM_3B42_Daily_7/summary)), ERA-5 data from the Copernicus data centre ([https://](https://cds.climate.copernicus.eu/cdsapp#!/dataset/reanalysis-era5-pressure-levels?tab=form)  
731 [cds.climate.copernicus.eu/cdsapp#!/dataset/reanalysis-era5-pressure-levels](https://cds.climate.copernicus.eu/cdsapp#!/dataset/reanalysis-era5-pressure-levels?tab=form)  
732 [?tab=form](https://cds.climate.copernicus.eu/cdsapp#!/dataset/reanalysis-era5-pressure-levels?tab=form)), and Tropflux data from the Indian National Centre for Ocean Information  
733 Services ([https://incois.gov.in/tropflux/data\\_access.jsp](https://incois.gov.in/tropflux/data_access.jsp)) and Nemo ocean model  
734 analysis with data from Copernicus data centre ([https://resources.marine.copernicus](https://resources.marine.copernicus.eu/?option=com_csw&view=details&product_id=GLOBAL_ANALYSIS_FORECAST_PHY_001_024)  
735 [.eu/?option=com\\_csw&view=details&product\\_id=GLOBAL\\_ANALYSIS\\_FORECAST\\_PHY\\_001](https://resources.marine.copernicus.eu/?option=com_csw&view=details&product_id=GLOBAL_ANALYSIS_FORECAST_PHY_001_024)  
736 [\\_024](https://resources.marine.copernicus.eu/?option=com_csw&view=details&product_id=GLOBAL_ANALYSIS_FORECAST_PHY_001_024)). The research presented in this paper was partially carried out on the High Per-  
737 formance Computing Cluster supported by the Research Computing Service at the Uni-  
738 versity of East Anglia.

739 **References**

- 740 Baranowski, D. B., Flatau, M. K., Flatau, P. J., Karnawati, D., Barabasz, K.,  
 741 Labuz, M., . . . Marzuki (2020). Social-media and newspaper reports re-  
 742 veal large-scale meteorological drivers of floods on Sumatra. *Nature Com-*  
 743 *munications*, *11*(1), 1–10. Retrieved from [http://dx.doi.org/10.1038/](http://dx.doi.org/10.1038/s41467-020-16171-2)  
 744 [s41467-020-16171-2](http://dx.doi.org/10.1038/s41467-020-16171-2) doi: 10.1038/s41467-020-16171-2
- 745 Baranowski, D. B., Flatau, M. K., Flatau, P. J., & Matthews, A. J. (2016a,  
 746 mar). Impact of atmospheric convectively coupled equatorial Kelvin waves  
 747 on upper ocean variability. *Journal of Geophysical Research*, *121*(5), 2045–  
 748 2059. Retrieved from <http://doi.wiley.com/10.1002/2015JD024150> doi:  
 749 10.1002/2015JD024150
- 750 Baranowski, D. B., Flatau, M. K., Flatau, P. J., & Matthews, A. J. (2016b). Phase  
 751 locking between atmospheric convectively coupled equatorial Kelvin waves and  
 752 the diurnal cycle of precipitation over the Maritime Continent. *Geophysical*  
 753 *Research Letters*, *43*(15), 8269–8276. doi: 10.1002/2016GL069602
- 754 Benschila, R., Durand, F., Masson, S., Bourdallé-Badie, R., de Boyer Montégut,  
 755 C., Papa, F., & Madec, G. (2014). The upper Bay of Bengal salinity  
 756 structure in a high-resolution model. *Ocean Modelling*, *74*, 36–52. Re-  
 757 trieved from <http://dx.doi.org/10.1016/j.ocemod.2013.12.001> doi:  
 758 10.1016/j.ocemod.2013.12.001
- 759 Birch, C. E., Webster, S., Peatman, S. C., Parker, D. J., Matthews, A. J., Li, Y.,  
 760 & Hassim, M. E. (2016). Scale interactions between the MJO and the  
 761 western Maritime Continent. *Journal of Climate*, *29*(7), 2471–2492. doi:  
 762 10.1175/JCLI-D-15-0557.1
- 763 Bray, N. A., Hautala, S., Chong, J., & Pariwono, J. (1996, may). Large-scale sea  
 764 level, thermocline, and wind variations in the Indonesian throughflow region.  
 765 *Journal of Geophysical Research: Oceans*, *101*(C5), 12239–12254. Retrieved  
 766 from <http://doi.wiley.com/10.1029/96JC00080> doi: 10.1029/96JC00080
- 767 Cane, M. A. (1984). Modeling Sea Level During El Niño. *Journal of Physi-*  
 768 *cal Oceanography*, *14*(12), 1864–1874. doi: 10.1175/1520-0485(1984)014<1864:  
 769 mslsden>2.0.co;2
- 770 de Boyer Montégut, C., Mignot, J., Lazar, A., & Cravatte, S. (2007). Control  
 771 of salinity on the mixed layer depth in the world ocean: 1. General de-

- 772            description.     *Journal of Geophysical Research: Oceans*, 112(6), 1–12.     doi:  
773            10.1029/2006JC003953
- 774   Dee, D. P., Uppala, S. M., Simmons, A. J., Berrisford, P., Poli, P., Kobayashi, S., ...  
775        Vitart, F. (2011). The ERA-Interim reanalysis: Configuration and performance  
776        of the data assimilation system. *Quarterly Journal of the Royal Meteorological*  
777        *Society*, 137(656), 553–597. doi: 10.1002/qj.828
- 778   DeMott, C. A., Klingaman, N. P., & Woolnough, S. J. (2015). Atmosphere-ocean  
779        coupled processes in the Madden-Julian oscillation. *Reviews of Geophysics*,  
780        53(4), 1099–1154. doi: 10.1002/2014RG000478
- 781   Drushka, K., Sprintall, J., & Gille, S. T. (2014, feb). Subseasonal variations in salin-  
782        ity and barrier-layer thickness in the eastern equatorial Indian Ocean. *Journal*  
783        *of Geophysical Research: Oceans*, 119(2), 805–823. Retrieved from [http://doi](http://doi.wiley.com/10.1002/2013JC009422)  
784        [.wiley.com/10.1002/2013JC009422](http://doi.wiley.com/10.1002/2013JC009422) doi: 10.1002/2013JC009422
- 785   Drushka, K., Sprintall, J., Gille, S. T., & Brodjonegoro, I. (2010). Vertical structure  
786        of Kelvin waves in the Indonesian throughflow exit passages. *Journal of Physi-*  
787        *cal Oceanography*, 40(9), 1965–1987. doi: 10.1175/2010JPO4380.1
- 788   Flatau, M., Flatau, P. J., Phoebus, P., & Niiler, P. P. (1997). The feedback be-  
789        tween equatorial convection and local radiative and evaporative processes:  
790        The implications for intraseasonal oscillations. *Journal of the Atmospheric*  
791        *Sciences*, 54(19), 2373–2386. doi: 10.1175/1520-0469(1997)054<2373:  
792        TFBECA>2.0.CO;2
- 793   Flatau, M. K., Flatau, P. J., Schmidt, J., & Kiladis, G. N. (2003). Delayed onset of  
794        the 2002 Indian monsoon. *Geophysical Research Letters*, 30(14), 28–31. doi: 10  
795        .1029/2003GL017434
- 796   Gill, A. (1980). Some simple solutions for heat-induced tropical circulation. *Quar-*  
797        *terly Journal of the Royal Meteorological Society*, 106(449), 447–462. doi: 10  
798        .1256/smsqj.44904
- 799   Godfrey, J. S., & Lindstrom, E. J. (1989). The heat budget of the equatorial western  
800        Pacific surface mixed layer. *Journal of Geophysical Research*, 94(C6), 8007.  
801        doi: 10.1029/jc094ic06p08007
- 802   Hagos, S., Foltz, G. R., Zhang, C., Thompson, E., Seo, H., Chen, S., ... Pro-  
803        tat, A. (2020). Atmospheric convection and air-sea interactions over the  
804        tropical oceans: Scientific progress, challenges, and opportunities. *Bul-*

- 805        *letin of the American Meteorological Society*, 101(3), E253–E258.        doi:  
806        10.1175/BAMS-D-19-0261.1
- 807        Halkides, D. J., Waliser, D. E., Lee, T., Menemenlis, D., & Guan, B. (2015). Quan-  
808        tifying the processes controlling intraseasonal mixed-layer temperature vari-  
809        ability in the tropical Indian Ocean. *Journal of Geophysical Research: Oceans*,  
810        120(2), 692–715. doi: 10.1002/2014JC010139
- 811        Han, W. (2005). Origins and Dynamics of the 90-Day and 3060-Day Variations  
812        in the Equatorial Indian Ocean. *Journal of Physical Oceanography*, 35(5),  
813        708–728. Retrieved from [http://journals.ametsoc.org/doi/abs/10.1175/  
814        JPO2725.1](http://journals.ametsoc.org/doi/abs/10.1175/JPO2725.1) doi: 10.1175/JPO2725.1
- 815        Han, W., Lawrence, D. M., & Webster, P. J. (2001). Dynamical response of equa-  
816        torial Indian Ocean to intraseasonal winds: Zonal flow. *Geophysical Research*  
817        *Letters*, 28(22), 4215–4218. doi: 10.1029/2001GL013701
- 818        Hersbach, H., Bell, B., Berrisford, P., Hirahara, S., Horányi, A., Muñoz-Sabater, J.,  
819        ... Thépaut, J. N. (2020). The ERA5 global reanalysis. *Quarterly Journal of*  
820        *the Royal Meteorological Society*, 146(730), 1999–2049. doi: 10.1002/qj.3803
- 821        Horii, T., Ueki, I., Syamsudin, F., Sofian, I., & Ando, K. (2016, apr). Intraseasonal  
822        coastal upwelling signal along the southern coast of Java observed using In-  
823        donesian tidal station data. *Journal of Geophysical Research: Oceans*, 121(4),  
824        2690–2708. Retrieved from [https://onlinelibrary.wiley.com/doi/abs/  
825        10.1002/2015JC010886](https://onlinelibrary.wiley.com/doi/abs/10.1002/2015JC010886) doi: 10.1002/2015JC010886
- 826        Huffman, G. J., Adler, R. F., Bolvin, D. T., Gu, G., Nelkin, E. J., Bowman,  
827        K. P., ... Wolff, D. B. (2007). The TRMM Multisatellite Precipitation  
828        Analysis (TMPA): Quasi-global, multiyear, combined-sensor precipitation  
829        estimates at fine scales. *Journal of Hydrometeorology*, 8(1), 38–55. doi:  
830        10.1175/JHM560.1
- 831        Inness, P. M., & Slingo, J. M. (2006). The interaction of the Madden-Julian Oscil-  
832        lation with the Maritime Continent in a GCM. *Quarterly Journal of the Royal*  
833        *Meteorological Society*, 132(618 A), 1645–1667. doi: 10.1256/qj.05.102
- 834        Iskandar, I., Mardiansyah, W., Masumoto, Y., & Yamagata, T. (2005). Intrasea-  
835        sonal Kelvin waves along the southern coast of Sumatra and Java. *Jour-  
836        nal of Geophysical Research C: Oceans*, 110(4), C04013–undefined. doi:  
837        10.1029/2004JC002508

- 838 Iskandar, I., & McPhaden, M. J. (2011). Dynamics of wind-forced intraseasonal  
 839 zonal current variations in the equatorial Indian Ocean. *Journal of Geophysical*  
 840 *Research: Oceans*, 116(6), C06019–undefined. doi: 10.1029/2010JC006864
- 841 Iskandar, I., Rao, S. A., & Tozuka, T. (2009). Chlorophyll-a bloom along the south-  
 842 ern coasts of Java and Sumatra during 2006. *International Journal of Remote*  
 843 *Sensing*, 30(3), 663–671. doi: 10.1080/01431160802372309
- 844 Kiladis, G. N., Wheeler, M. C., Haertel, P. T., Straub, K. H., & Roundy, P. E.  
 845 (2009, apr). Convectively coupled equatorial waves. *Reviews of Geo-*  
 846 *physics*, 47(2), RG2003. Retrieved from [http://doi.wiley.com/10.1029/](http://doi.wiley.com/10.1029/2008RG000266)  
 847 [2008RG000266](http://doi.wiley.com/10.1029/2008RG000266) doi: 10.1029/2008RG000266
- 848 Kumar, B. P., Vialard, J., Lengaigne, M., Murty, V. S., & McPhaden, M. J. (2012).  
 849 TropFlux: Air-sea fluxes for the global tropical oceans-description and evalua-  
 850 tion. *Climate Dynamics*, 38(7-8), 1521–1543. doi: 10.1007/s00382-011-1115-0
- 851 Ling, J., Zhang, C., Joyce, R., Xie, P., & Chen, G. (2019, mar). Possible Role of  
 852 the Diurnal Cycle in Land Convection in the Barrier Effect on the MJO by  
 853 the Maritime Continent. *Geophysical Research Letters*, 46(5), 3001–3011.  
 854 Retrieved from [https://onlinelibrary.wiley.com/doi/abs/10.1029/](https://onlinelibrary.wiley.com/doi/abs/10.1029/2019GL081962)  
 855 [2019GL081962](https://onlinelibrary.wiley.com/doi/abs/10.1029/2019GL081962) doi: 10.1029/2019GL081962
- 856 Madden, R. A., & Julian, P. R. (1971, jul). Detection of a 4050 Day Oscillation in  
 857 the Zonal Wind in the Tropical Pacific. *Journal of the Atmospheric Sciences*,  
 858 28(5), 702–708. Retrieved from [http://journals.ametsoc.org/doi/abs/](http://journals.ametsoc.org/doi/abs/10.1175/1520-0469(1971)028<0702:DOADOI>2.0.CO;2)  
 859 [10.1175/1520-0469\(1971\)028<0702:DOADOI>2.0.CO;2](http://journals.ametsoc.org/doi/abs/10.1175/1520-0469(1971)028<0702:DOADOI>2.0.CO;2)  
 860 [.0.CO;2](http://journals.ametsoc.org/doi/abs/10.1175/1520-0469(1971)028<0702:DOADOI>2.0.CO;2) doi: 10.1175/1520-0469(1971)028(0702:DOADOI)2.0.CO;2
- 861 Madec, G. (2008). Nemo ocean engine. *Note du P<sup>ole</sup> de modélisation, Institut*  
 862 *Pierre-Simon Laplace (IPSL)*, 27, 219.
- 863 Majda, A. J., Khouider, B., Kiladis, G. N., Straub, K. H., & Shefter, M. G. (2004).  
 864 A model for convectively coupled tropical waves: Nonlinearity, rotation, and  
 865 comparison with observations. *Journal of the Atmospheric Sciences*, 61(17),  
 866 2188–2205. doi: 10.1175/1520-0469(2004)061<2188:AMFCCT>2.0.CO;2
- 867 Mapes, B., Tulich, S., Lin, J., & Zuidema, P. (2006). The mesoscale convection  
 868 life cycle: Building block or prototype for large-scale tropical waves? *Dynamics*  
 869 *of Atmospheres and Oceans*, 42(1-4), 3–29. doi: 10.1016/j.dynatmoce.2006.03  
 870 .003

- 871 Masson, S., Delecluse, P., Boulanger, J.-P., & Menkes, C. (2002, dec). A model  
 872 study of the seasonal variability and formation mechanisms of the barrier  
 873 layer in the eastern equatorial Indian Ocean. *Journal of Geophysical Re-*  
 874 *search: Oceans*, 107(C12), SRF 18–1–SRF 18–20. Retrieved from [http://](http://doi.wiley.com/10.1029/2001JC000832)  
 875 [doi.wiley.com/10.1029/2001JC000832](http://doi.wiley.com/10.1029/2001JC000832) doi: 10.1029/2001JC000832
- 876 Matthews, A. J. (2000). Propagation mechanisms for the Madden-Julian Oscilla-  
 877 tion. *Quarterly Journal of the Royal Meteorological Society*, 126(569), 2637–  
 878 2651. doi: 10.1256/smsqj.56901
- 879 Matthews, A. J., Singhruck, P., & Heywood, K. J. (2010). Ocean temperature and  
 880 salinity components of the Madden-Julian oscillation observed by Argo floats.  
 881 *Climate Dynamics*, 35(7), 1149–1168. doi: 10.1007/s00382-009-0631-7
- 882 McCreary, Jr., J. P. (1984, may). Equatorial beams. *Journal of Marine Research*,  
 883 42(2), 395–430. Retrieved from [http://openurl.ingenta.com/content/](http://openurl.ingenta.com/content/xref?genre=article&iissn=0022-2402&volume=42&issue=2&spage=395)  
 884 [xref?genre=article&iissn=0022-2402&volume=42&issue=](http://openurl.ingenta.com/content/xref?genre=article&iissn=0022-2402&volume=42&issue=2&spage=395)  
 885 [2&spage=395](http://openurl.ingenta.com/content/xref?genre=article&iissn=0022-2402&volume=42&issue=2&spage=395) doi: 10.1357/002224084788502792
- 886 McDougall, T. J., & Barker, P. M. (2011). *Getting started with TEO-10 and the*  
 887 *Gibbs Seawarer Oceanographic Toolbox*. SCOR/IAPSO WG127. Retrieved from  
 888 <http://www.teos-10.org/>
- 889 Meehl, M., Lukas, R., Kiladis, G. N., Weickmann, K. M., Matthews, A. J., &  
 890 Wheeler, M. (2001). A conceptual framework for time and space scale in-  
 891 teractions in the climate system. *Climate Dynamics*, 17(10), 753–775. doi:  
 892 10.1007/s003820000143
- 893 Moore, D. W., & McCreary, J. P. (1990). Excitation of intermediate-frequency  
 894 equatorial waves at a western ocean boundary: With application to observa-  
 895 tions from the Indian Ocean. *Journal of Geophysical Research*, 95(C4), 5219.  
 896 Retrieved from <http://doi.wiley.com/10.1029/JC095iC04p05219> doi:  
 897 10.1029/JC095iC04p05219
- 898 Moum, J. N., De Szoeke, S. P., Smyth, W. D., Edson, J. B., DeWitt, H. L., Moulin,  
 899 A. J., . . . Fairall, C. W. (2014). Air-sea interactions from westerly wind bursts  
 900 during the november 2011 MJO in the Indian Ocean. *Bulletin of the American*  
 901 *Meteorological Society*, 95(8), 1185–1199. doi: 10.1175/BAMS-D-12-00225.1
- 902 Moum, J. N., Pujiana, K., Lien, R. C., & Smyth, W. D. (2016). Ocean feedback to  
 903 pulses of the Madden-Julian Oscillation in the equatorial Indian Ocean. *Nature*

- 904        *Communications*, 7(May), 1–7. Retrieved from [http://dx.doi.org/10.1038/](http://dx.doi.org/10.1038/ncomms13203)  
 905        ncomms13203 doi: 10.1038/ncomms13203
- 906 Nagura, M., & McPhaden, M. J. (2012). The dynamics of wind-driven intraseasonal  
 907        variability in the equatorial Indian Ocean. *Journal of Geophysical Research:*  
 908        *Oceans*, 117(2), 1–16. doi: 10.1029/2011JC007405
- 909 Nagura, M., & Mcphaden, M. J. (2018). The shallow overturning circulation in  
 910        the Indian Ocean. *Journal of Physical Oceanography*, 48(2), 413–434. doi: 10  
 911        .1175/jpo-d-17-0127.1
- 912 Potemra, J. T., Hacker, P. W., Melnichenko, O., & Maximenko, N. (2016, jul).  
 913        Satellite estimate of freshwater exchange between the Indonesian Seas and  
 914        the Indian Ocean via the Sunda Strait. *Journal of Geophysical Research:*  
 915        *Oceans*, 121(7), 5098–5111. Retrieved from [http://doi.wiley.com/10.1002/](http://doi.wiley.com/10.1002/2015JC011618)  
 916        2015JC011618[https://onlinelibrary.wiley.com/doi/abs/10.1002/](https://onlinelibrary.wiley.com/doi/abs/10.1002/2015JC011618)  
 917        2015JC011618 doi: 10.1002/2015JC011618
- 918 Prasad, T. G., & Ikeda, M. (2002). The wintertime water mass formation in the  
 919        Northern Arabian Sea: A model study. *Journal of Physical Oceanography*,  
 920        32(3), 1028–1040. doi: 10.1175/1520-0485(2002)032<1028:TWWMF1>2.0.CO;  
 921        2
- 922 Pujiana, K., & McPhaden, M. J. (2018). Ocean Surface Layer Response to  
 923        Convectively Coupled Kelvin Waves in the Eastern Equatorial Indian  
 924        Ocean. *Journal of Geophysical Research: Oceans*, 123(8), 5727–5741. doi:  
 925        10.1029/2018JC013858
- 926 Pujiana, K., & McPhaden, M. J. (2020). Intraseasonal Kelvin Waves in the Equa-  
 927        torial Indian Ocean and their Propagation into the Indonesian Seas. *Journal of*  
 928        *Geophysical Research: Oceans*, 125(5), 1–18. doi: 10.1029/2019jc015839
- 929 Rao, S. A., & Yamagata, T. (2004). Abrupt termination of Indian Ocean dipole  
 930        events in response to intraseasonal disturbances. *Geophysical Research Letters*,  
 931        31(19), 1–4. doi: 10.1029/2004GL020842
- 932 Roundy, P. E. (2008). Analysis of convectively coupled Kelvin waves in the Indian  
 933        ocean MJO. *Journal of the Atmospheric Sciences*, 65(4), 1342–1359. doi: 10  
 934        .1175/2007JAS2345.1
- 935 Rydbeck, A. V., & Jensen, T. G. (2017). Oceanic impetus for convective onset of  
 936        the Madden-Julian oscillation in the western Indian ocean. *Journal of Climate*,

- 937           30(11), 4299–4316. doi: 10.1175/JCLI-D-16-0595.1
- 938 Schott, F. A., Xie, S.-P., & McCreary Jr, J. P. (2009). Indian Ocean Circulation  
939 and Climate Variability. *Reviews of Geophysics*, 47(2007), 1–46. Retrieved  
940 from <http://www.agu.org/pubs/crossref/2009/2007RG000245.shtml> doi:  
941 10.1029/2007RG000245.1
- 942 Shinoda, T., Hendon, H. H., & Glick, J. (1998). Intraseasonal Variability of  
943 Surface Fluxes and Sea Surface Temperature in the Tropical Western Pa-  
944 cific and Indian Oceans. *Journal of Climate*, 11(7), 1685–1702. doi:  
945 10.1175/1520-0442(1998)011<1685:IVOSFA>2.0.CO;2
- 946 Sprintall, J., & Tomczak, M. (1992). Evidence of the Barrier Layer in the Surface  
947 Layer of the Tropics ocean surface mixed layer generally denotes a quasi-ki-  
948 netic energy and potential energy processes mentioned its degree state. *Journal*  
949 *Of Geophysical Research*, 97(C5), 7305–7316.
- 950 Susanto, R. D., Gordon, A. L., & Zheng, Q. (2001). Upwelling along the coasts  
951 of Java and Sumatra and its relation to ENSO. *Geophysical Research Letters*,  
952 28(8), 1599–1602. doi: 10.1029/2000GL011844
- 953 Syamsudin, F., Kaneko, A., & Haidvogel, D. B. (2004). Numerical and observational  
954 estimates of Indian Ocean Kelvin wave intrusion into Lombok Strait. *Geophys-*  
955 *ical Research Letters*, 31(24), 1–4. doi: 10.1029/2004GL021227
- 956 Webber, B. G. M., Matthews, A. J., & Heywood, K. J. (2010). A dynamical ocean  
957 feedback mechanism for the Madden-Julian Oscillation. *Quarterly Journal of*  
958 *the Royal Meteorological Society*, 136(648), 740–754. doi: 10.1002/qj.604
- 959 Webber, B. G. M., Matthews, A. J., Heywood, K. J., Kaiser, J., & Schmidtko, S.  
960 (2014, jun). Seaglider observations of equatorial Indian Ocean Rossby waves  
961 associated with the Madden-Julian Oscillation. *Journal of Geophysical Re-*  
962 *search: Oceans*, 119(6), 3714–3731. Retrieved from [http://doi.wiley.com/](http://doi.wiley.com/10.1002/2013JC009657)  
963 10.1002/2013JC009657 doi: 10.1002/2013JC009657
- 964 Webber, B. G. M., Matthews, A. J., Heywood, K. J., & Stevens, D. P. (2012).  
965 Ocean Rossby waves as a triggering mechanism for primary Madden-Julian  
966 events. *Quarterly Journal of the Royal Meteorological Society*, 138(663), 514–  
967 527. doi: 10.1002/qj.936
- 968 Wheeler, M., & Kiladis, G. N. (1999). Convectively Coupled Equatorial  
969 Waves: Analysis of Clouds and Temperature in the Wavenumber-Frequency

- 970 Domain. *Journal of the Atmospheric Sciences*, 56(3), 374–399. doi:  
971 10.1175/1520-0469(1999)056<0374:CCEWAO>2.0.CO;2
- 972 Wheeler, M., Kiladis, G. N., & Webster, P. J. (2000). Large-scale dynamical fields  
973 associated with convectively coupled equatorial waves. *Journal of the At-*  
974 *mospheric Sciences*, 57(5), 613–640. doi: 10.1175/1520-0469(2000)057<0613:  
975 LSDFAW>2.0.CO;2
- 976 Wyrski, K. (1962). The upwelling in the region between Java and Australia during  
977 the south-east monsoon. *Australian journal of marine and freshwater research*,  
978 13, 217–225. Retrieved from [http://hdl.handle.net/102.100.100/329922](http://hdl.handle.net/102.100.100/329922?index=1)  
979 ?index=1 doi: procite:751a1915-67ee-42ba-9121-4eaf8d1b8985
- 980 Zhang, C. (2005). Madden-Julian Oscillation. *Reviews of Geophysics*, 43(2), 1–36.  
981 Retrieved from [http://140.90.101.29/products/precip/CWlink/MJO/MJO{\\\_}](http://140.90.101.29/products/precip/CWlink/MJO/MJO{\_}1page{\_}factsheet.pdf)  
982 [\\_}1page{\\\_}factsheet.pdf](http://140.90.101.29/products/precip/CWlink/MJO/MJO{\_}1page{\_}factsheet.pdf)<http://doi.wiley.com/10.1029/2004RG000158>  
983 doi: 10.1029/2004RG000158

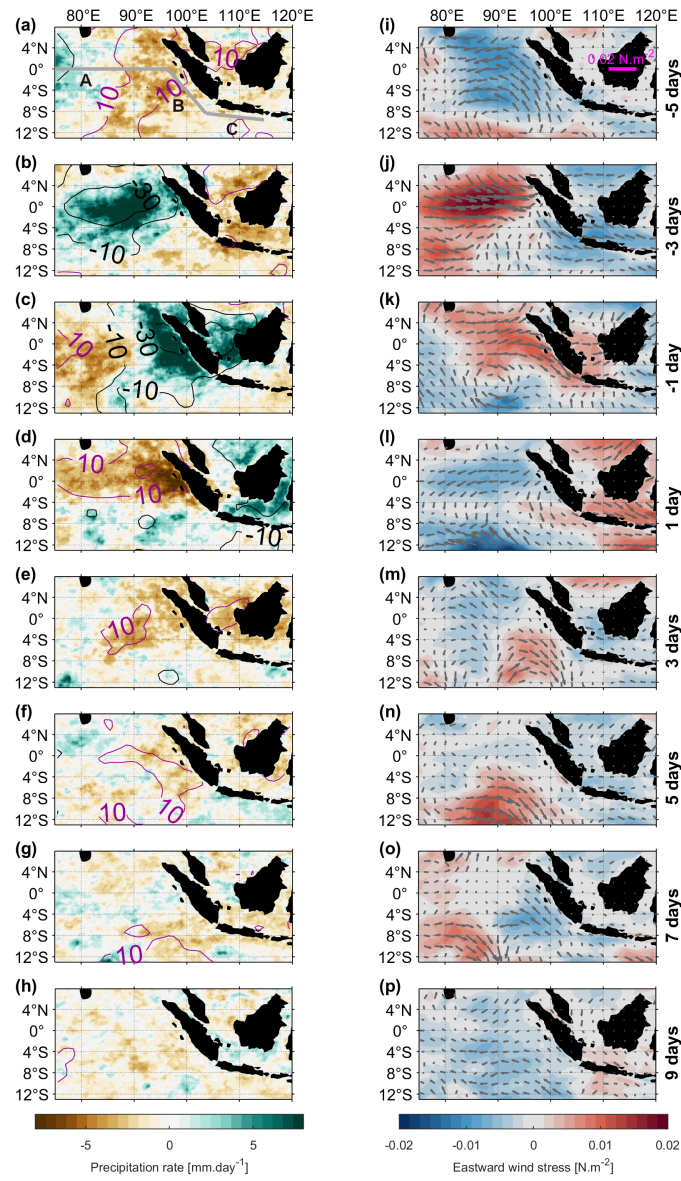


**Figure 1.** Lagged composite anomalies of: (a–h) precipitation rate ( $\text{mm day}^{-1}$ , colour shaded) and net heat flux (contour interval is  $20 \text{ W m}^{-2}$ ; negative contours are black, positive contours are magenta, and the first positive contour is at  $10 \text{ W m}^{-2}$ ); (i–p) eastward wind stress ( $\text{N m}^{-2}$ ; colour shaded) and wind stress vectors ( $\text{N m}^{-2}$ ; reference vector in panel i), for strong solitary CCKW events passing the  $110^\circ \text{ E}$  base point at lag 0.

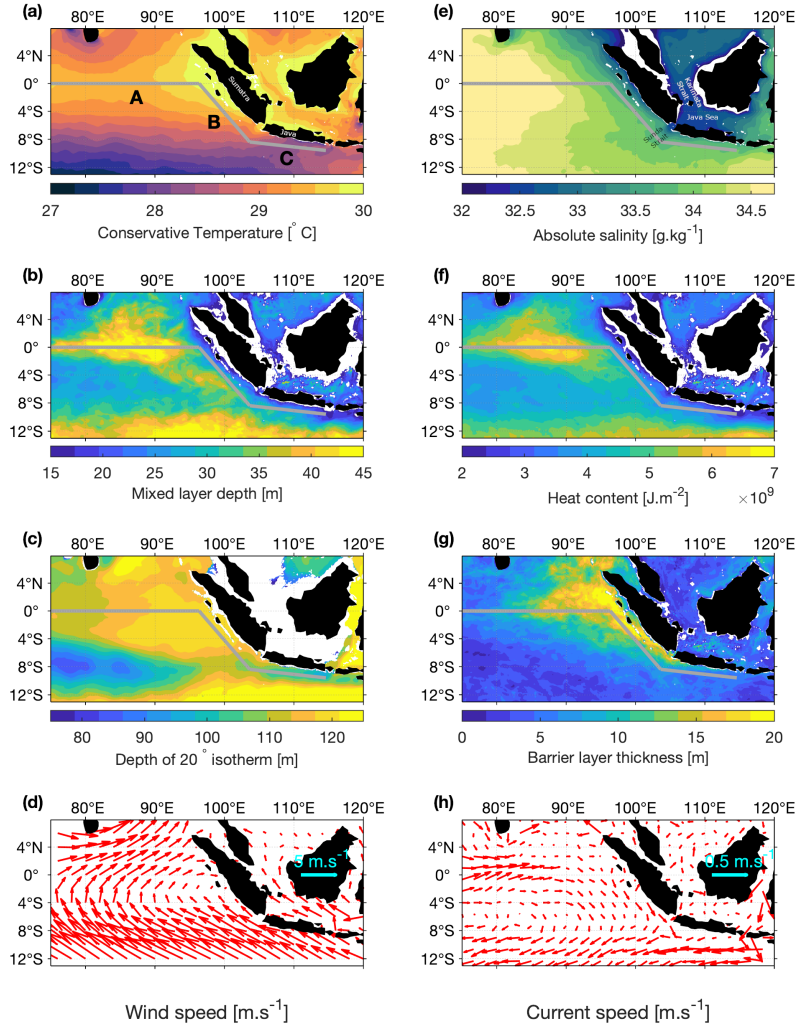


**Figure 2.** Precursor fields (composite means over lags  $-10$  to  $-6$  days, relative to CCKW events crossing  $110^\circ$  at lag 0 days) of (a) oceanic conservative temperature ( $^\circ\text{C}$ ), (b) mixed layer depth (m), (c) depth of the  $20^\circ\text{C}$  isotherm, (d) surface wind vectors  $\text{m s}^{-1}$ , (e) absolute salinity ( $\text{g kg}^{-1}$ ), (f) heat content  $\text{J m}^{-2}$ , (g) barrier layer thickness (m) and (h) surface ocean current vectors  $\text{m s}^{-1}$ . The grey lines shows the propagation path of oceanic Kelvin waves and consist of three sections labelled in panel (a): section A along the Equator from  $60^\circ\text{E}$  to  $96.35^\circ\text{E}$ ; section B along the coast of Sumatra, and section C along the coast of Java.

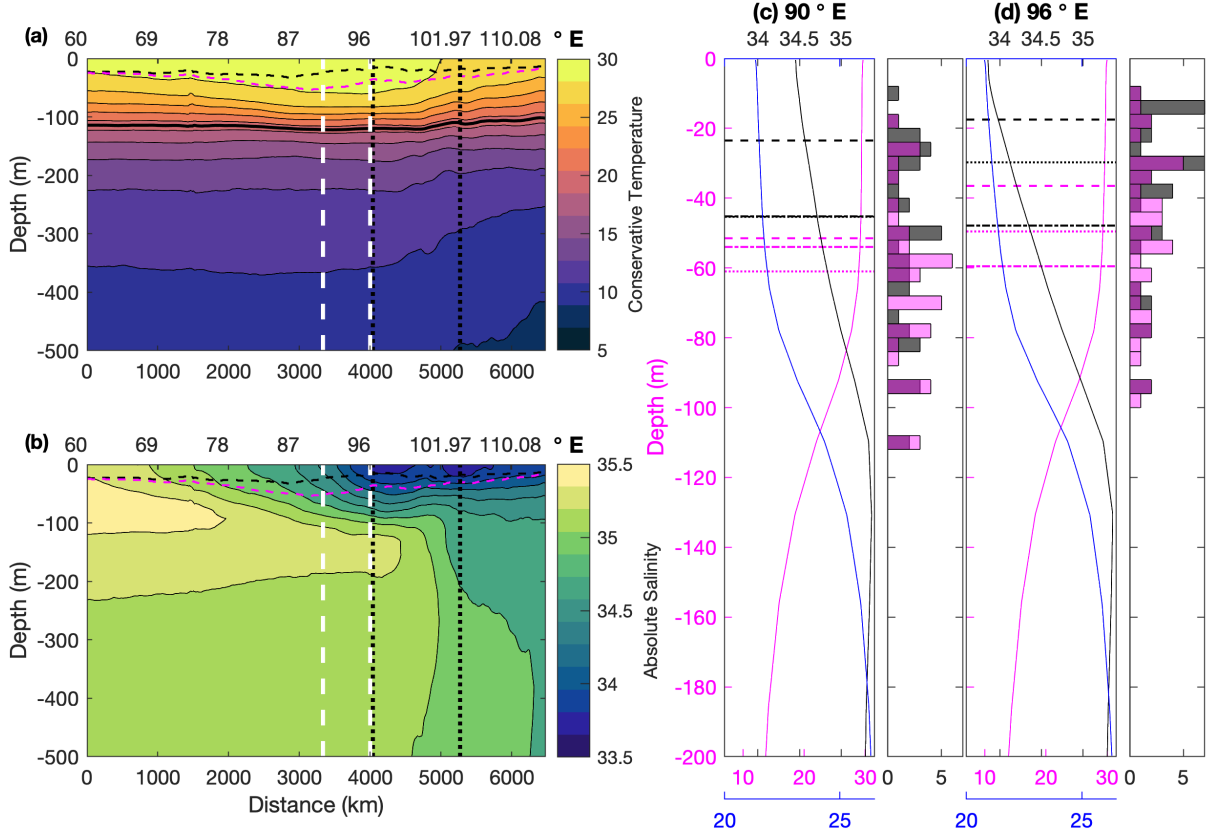


**Figure 3.** Precursor fields (defined as in Fig. 2) of (a) conservative temperature ( $^{\circ}\text{C}$ ; contoured between  $15^{\circ}\text{C}$  and  $29^{\circ}\text{C}$ , every  $2^{\circ}\text{C}$ , with extra level at  $20^{\circ}\text{C}$  (thick line). (b) absolute salinity ( $\text{g kg}^{-1}$ ; contoured between  $32 \text{ g kg}^{-1}$  and  $35.4 \text{ g kg}^{-1}$  every  $0.2 \text{ g kg}^{-1}$ ) along vertical ocean sections A, B and C (limit of section indicated by vertical black dotted lines; see map in figure 2a for geographic reference). Bottom horizontal axis shows distance from the  $60^{\circ}\text{E}$  meridian and top horizontal axis indicates longitude. Black and magenta dashed lines indicate mixed layer depth (MLD) and isothermal layer depth (ILD) calculated from the averaged profile, respectively. White vertical dashed lines indicate the position of profiles at  $90^{\circ}\text{E}$  and  $96^{\circ}\text{E}$ . Panels (c) and (d) show profile of conservative temperature ( $^{\circ}\text{C}$ ; magenta), absolute salinity ( $\text{g kg}^{-1}$ ; black) and potential density ( $\text{kg m}^{-3}$ ; blue) at  $90^{\circ}\text{E}$  and  $96^{\circ}\text{E}$ , respectively. Black and magenta horizontal lines indicate MLD and ILD, calculated from the averaged M10-M6 composite profiles (dashed lines), from averaging the M10-M6 composite values of MLD and ILD (dotted lines), and from averaging the climatological daily MLD and ILD values (dotted-dash line). Histograms show the daily MLD (black) and ILD (magenta) values at day zero for all solitary events. ILD (magenta) histogram is presented with a 50% colour transparency level and plotted on top of the MLD histogram.

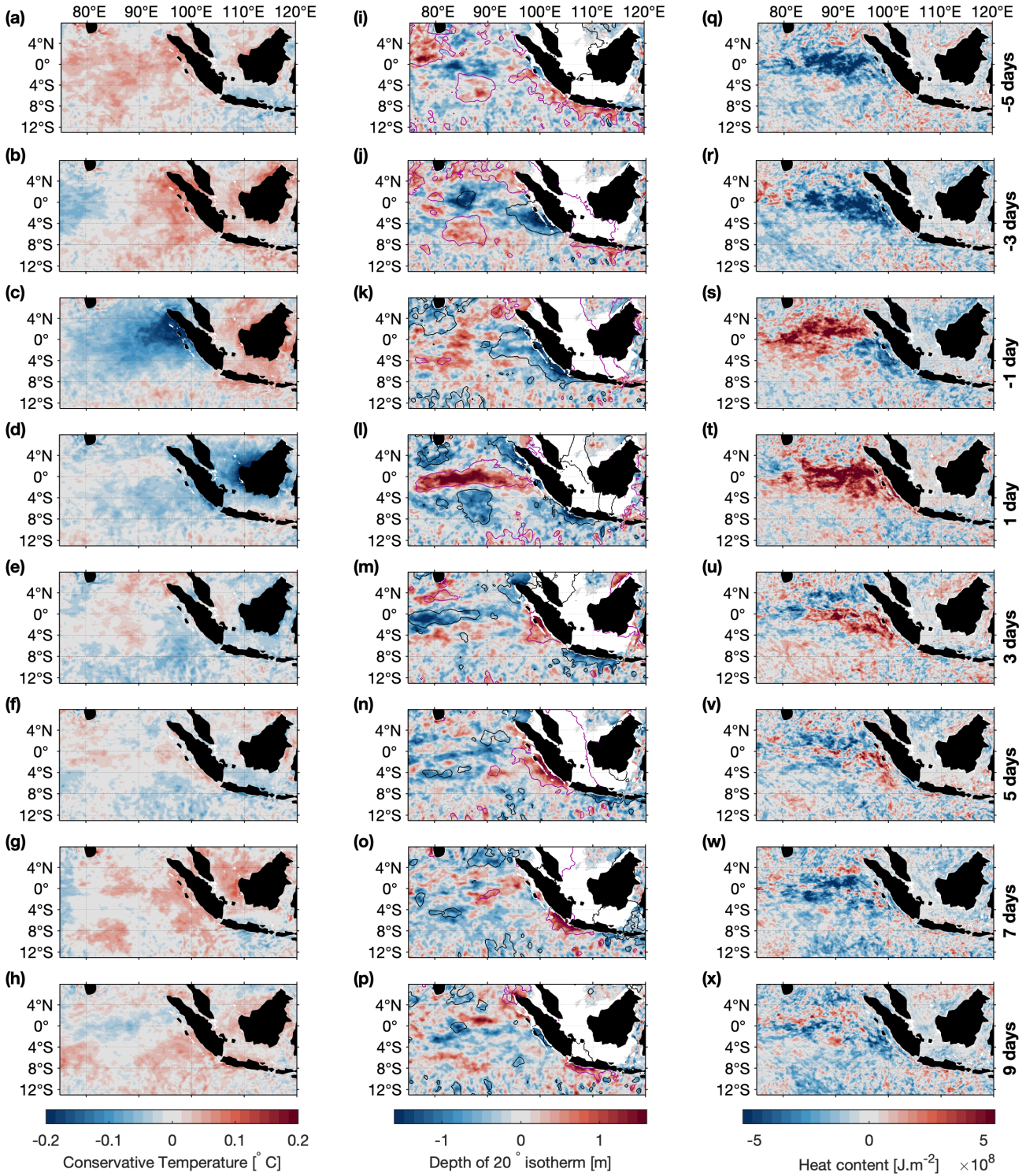


**Figure 4.** Maps of daily lagged composite anomalies of (a-h) sea surface conservative temperature (°C; colour shaded); (i-p) depth of 20 °C isotherm (m; colour shaded) and sea surface height (m; contoured at the intervals -0.01, -0.003, 0.003, 0.01); (q-x) heat content of the mixed layer (J m<sup>-2</sup>; colour shaded) for CCKW strong solitary events passing at 110°E at lag 0. For all panels negative values are contoured in black lines and positive values in magenta lines.

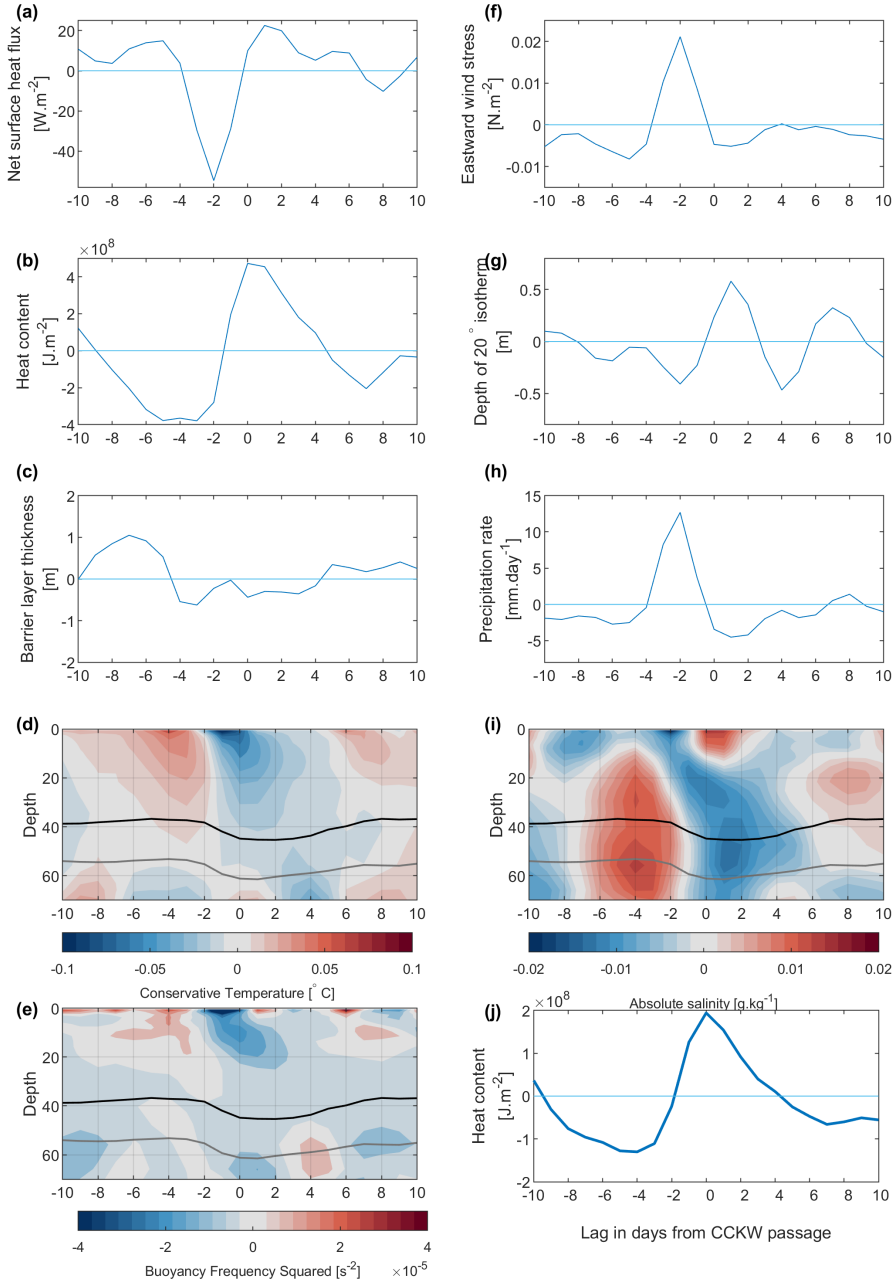


**Figure 5.** Daily composite anomalies averaged over a box in the equatorial Indian Ocean ( $2.5^{\circ}\text{N}$ – $2.5^{\circ}\text{S}$ ,  $90^{\circ}\text{E}$ – $95^{\circ}\text{E}$ ) for (a) net surface heat flux, (b) heat content, (c) barrier layer thickness, (d) conservative temperature, (e) buoyancy frequency squared, (f) eastward wind stress, (g) depth of  $20^{\circ}\text{C}$  isotherm, (h) precipitation rate and (i) absolute salinity. In panel (d), mixed layer depth (MLD) is shown by the black line, and isopycnal layer depth (ILD) by the gray line. In panel (j), daily composites of heat content anomaly are shown averaged over the larger domain  $8^{\circ}\text{S}$ – $4^{\circ}\text{N}$ ,  $75$ – $100^{\circ}\text{E}$ .

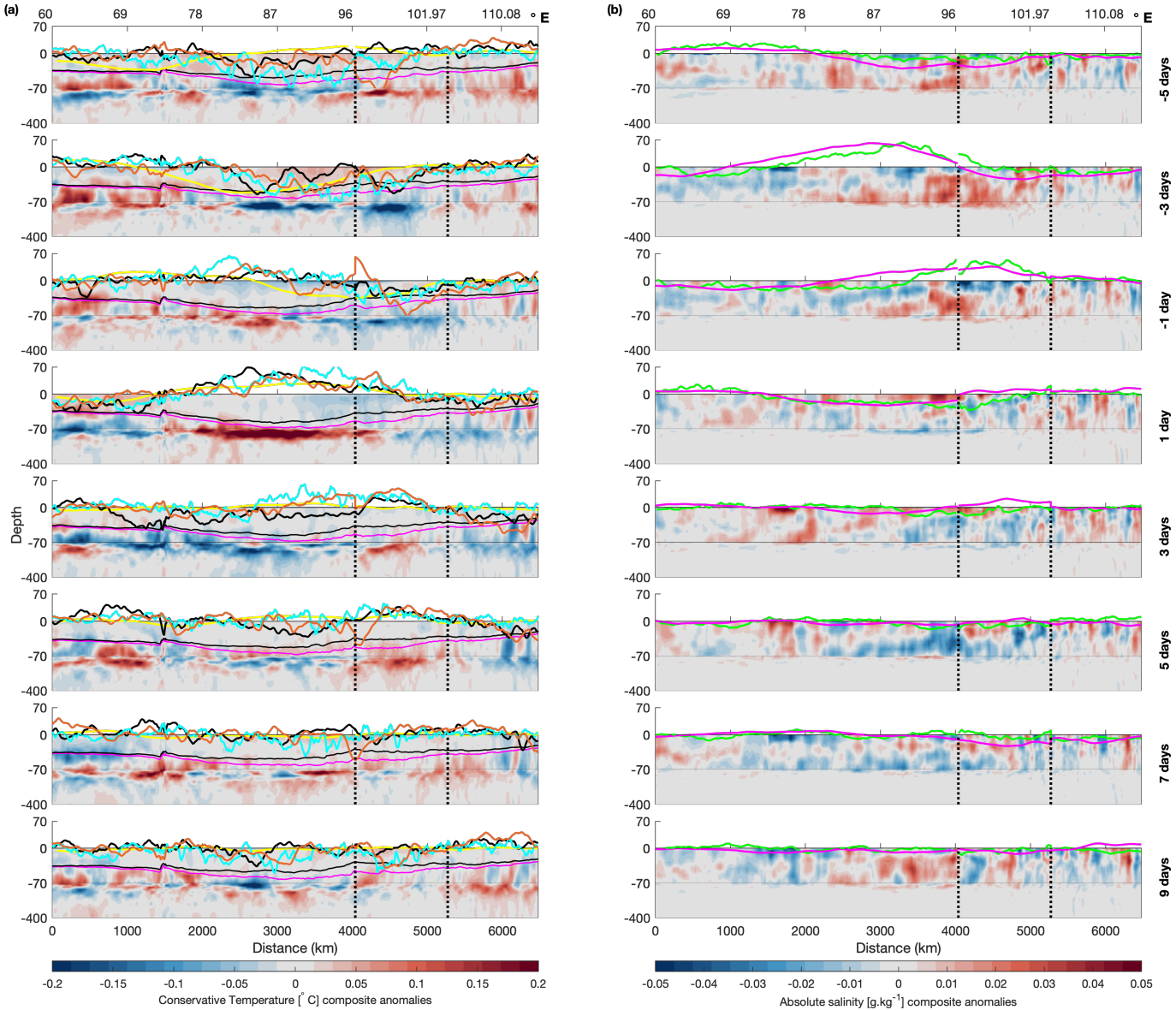


**Figure 6.** Vertical section (sections A, B and C, limits indicated by vertical dotted line; see map in Figure 2) of daily lagged composite anomalies at lags  $-5$ ,  $-3$ ,  $-1$ ,  $+1$ ,  $+3$ ,  $+5$ ,  $+7$  and  $+9$  of (a) conservative temperature ( $^{\circ}\text{C}$ ) and (b) absolute salinity ( $\text{g kg}^{-1}$ ) for CCKW strong solitary events passing at  $110^{\circ}\text{E}$ . In panels (a), daily composites of MLD and ILD total fields are shown by black and magenta lines, respectively. Along section daily composites of anomaly fields of downward net heat flux ( $\times 2$ ;  $\text{W m}^{-2}$ ; yellow line), depth of  $20^{\circ}\text{C}$  isotherm ( $\times 20$ ; m; black line, heat content ( $\times 10^{-7}$ ;  $\text{J m}^{-2}$ ; cyan line) and ocean velocity parallel to the sections ( $\times 3.10^3$ ;  $\text{m s}^{-1}$ ; brown line). In panels (b) it is shown the along section daily composites of anomaly fields of precipitation ( $\times 4.5$ ;  $\text{mm day}^{-1}$ ; green line) and wind stress parallel to the sections ( $\times 2.5.10^3$ ;  $\text{N m}^{-2}$ ; magenta line). Note that the scale of the vertical axis is different for the range from 70 to  $-70$  and that from  $-400$  to  $-70$ .

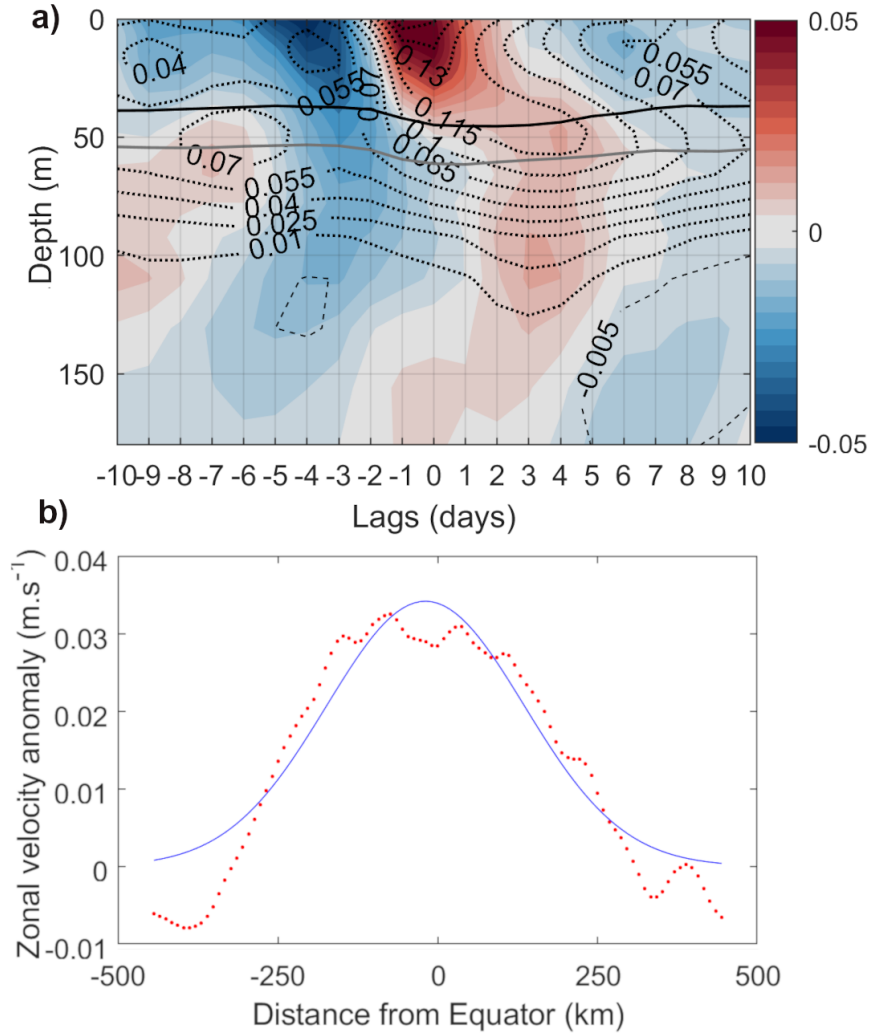


**Figure 7.** (a) Zonal velocity ( $\text{m}\cdot\text{s}^{-1}$ ) composite anomalies (colour shading), and total field (dotted line contours), averaged over  $2.5^{\circ}\text{S}$ – $2.5^{\circ}\text{N}$ ,  $90$ – $95^{\circ}\text{E}$ . Thick black and gray lines indicates the MLD and ILD respectively. (b) Zonal velocity anomalies ( $\text{m}\cdot\text{s}^{-1}$ ; red circles) averaged between  $100$ – $200$  m for lag  $+3$  days using  $90^{\circ}\text{E}$  as the CCKW composite base point between  $4^{\circ}\text{N}$ – $4^{\circ}\text{S}$ . Data are 90-day high-pass filtered. The blue line shows the best least-square fit to a theoretical Kelvin wave solution.

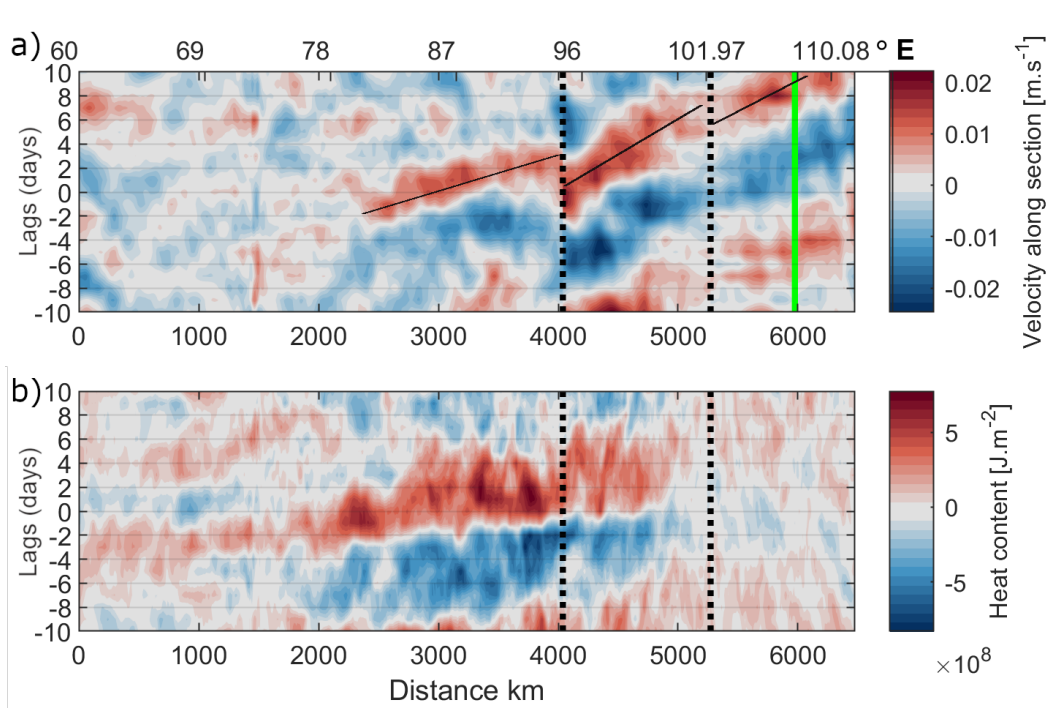


**Figure 8.** Hovmöller diagram for daily composite anomalies for (a) zonal velocity ( $\text{m s}^{-1}$ ) (60–200 m average), (b) depth of  $20^\circ\text{C}$  isotherm (m) and (c) heat content ( $\text{J m}^{-2}$ ) along sections A, B and C (section limits indicated by vertical dotted lines; see map in Figure 2). Vertical green line indicates base point location for composite calculations.